Journal of Computational Physics 523 (2025) 113667

Contents lists available at ScienceDirect

Journal of Computational Physics

journal homepage: www.elsevier.com/locate/jcp

One-side diffuse-interface immersed boundary method for compressible flows

Buchen Wu [a], Yaguang Liu [d], Lin Fu [a,b,c,*]

[a] Department of Mechanical and Aerospace Engineering, The Hong Kong University of Science and Technology, Clear Water Bay, Kowloon, Hong Kong
[b] Department of Mathematics, The Hong Kong University of Science and Technology, Clear Water Bay, Kowloon, Hong Kong
[c] HKUST Shenzhen-Hong Kong Collaborative Innovation Research Institute, Futian, Shenzhen, China
[d] Department of Mechanics and Aerospace Engineering, Southern University of Science and Technology, Shenzhen 518055, Guangdong, China

ARTICLE INFO

Keywords:
Immersed boundary method
Continuous forcing
Diffuse interface method
Compressible flows

ABSTRACT

In this work, within the framework of the continuous forcing immersed boundary method (IBM), a novel one-side diffuse-interface IBM is proposed for the simulation of compressible viscous flows around complex geometries, where the flow corrections are implicitly evaluated by solving two linear systems to accurately satisfy the Dirichlet and Neumann boundary conditions. Moreover, the Lagrangian corrections are biasedly distributed on the Eulerian points inside the solid domain through a novel spreading scheme, which effectively eliminates the diffusion effects introduced by the regularization delta function. Consequently, the non-physical pressure jump in the traditional continuous forcing IBM around the immersed object is eradicated. The instantaneous discretization errors of the Dirichlet and Neumann boundary conditions are negligible and close to the machine round-off, indicating that the pressure and thermal boundary conditions are accurately enforced on the immersed object. The proposed diffuse interface IBM integrated with the gas kinetic flux solver (GKFS) can achieve a second-order discretization accuracy in space. The proposed numerical approach is validated with several classical benchmarks, and the results agree well with those of the sharp interface method and body-fitted approach, demonstrating that the proposed diffuse interface IBM can accurately predict the flow characteristics around the immersed object, such as the shockwave locations, the pressure and temperature distributions. Moreover, the proposed diffuse interface IBM is extended to simulate compressible viscous flows around the immersed object with complex geometries, where good agreements between the present results and the body-fitted results are achieved as well.

1. Introduction

Due to the significant demands arising in scientific and engineering communities, computational fluid dynamics (CFD) have been greatly developed in recent decades for solving practical problems in various engineering areas, such as aerospace engineering, ocean engineering and wind engineering. The conventional CFD numerical approaches solve problems with body-fitted meshes to achieve high numerical accuracy, where the boundary conditions are implemented through specifying desired boundary values on

* Corresponding author at: Department of Mechanical and Aerospace Engineering, The Hong Kong University of Science and Technology, Clear Water Bay, Kowloon, Hong Kong.
E-mail address: linfu@ust.hk (L. Fu).

https://doi.org/10.1016/j.jcp.2024.113667
Received 18 June 2024; Received in revised form 4 November 2024; Accepted 7 December 2024

Available online 11 December 2024

the first layer of nodes on the solid surface. However, for complex solid geometries, generating high-quality body-fitted meshes requires complex mesh-generation techniques. Differing from the conventional numerical approaches employing body-fitted meshes, immersed boundary method (IBM) provides an alternative approach by converting the solid boundary effects into the forcing source terms in the governing equations, indicating that this numerical method circumvents the need to regenerate meshes for different geometries.

The methodology of IBM is firstly proposed by Peskin [1] for simulating blood flows in the human heart. Subsequently, many IBMs have been developed to accurately enforce boundary conditions on the immersed objects based on different physical models, for example, the penalty forcing IBM [2,3], the feedback forcing IBM [4,5], the direct forcing IBM [6–11], the multi-direct forcing IBM [12–15] and velocity-correction IBM [16–19]. Based on the restoring force spreading process, IBMs can be categorized into two groups: diffuse interface method (continuous forcing) and sharp interface method (discrete forcing) [20]. The diffuse interface IBMs have been widely applied for simulating incompressible flows past solid objects with complex geometries, where the IBMs are mainly adopted to enforce the Dirichlet boundary condition [21–24]. On the other hand, the sharp interface IBMs are widely employed to simulate compressible flows, because the sharp interface method can accurately describe the immersed boundary without diffusion effects. There are several distinctive sharp interface IBMs, such as the immersed interface methods [25–27], the cut-cell based IBMs [28–30] and the ghost cell based IBMs [31–33]. However, when tackling flow problems with complex geometries, the sharp interface methods may encounter some numerical problems. For instance, the small cut-cells induce severe numerical instability within cut-cell IBMs, and the ghost cell IBMs need to identify different points around solid boundary using complex point identification algorithm and construct different interpolation/extrapolation stencils for different geometries. These numerical issues are obstacles for applying the sharp interface methods to simulate compressible problems with complex geometries. Therefore, an alternative idea is to extend the diffuse interface IBM for simulating compressible viscous flows, due to its implementation simplicity and numerical robustness. Qiu et al. [34] extend the velocity-correction IBM proposed by Wu and Shu [16] to simulate compressible flow, where they firstly calculate the momentum corrections and then evaluate the density corrections through the continuity equation. Subsequently, Wang et al. [35] apply the feedback forcing IBM to simulate the compressible multiphase flows, where the IBM restoring force is only added to the momentum equation. Sun et al. [36] adopt the velocity-correction IBM to enforce the no-slip and thermal boundary conditions, where they propose an iterative technique to evaluate the density corrections for enforcing the continuity equation. Riahi et al. [37] propose a pressure-corrected IBM for compressible flows, where the implicit direct forcing IBM is employed to enforce the Dirichlet boundary condition and the pressure-correction is derived from the momentum equation to ensure the pressure gradient around the solid interface is consistent with the homogeneous Neumann boundary condition. Yu and Pantano [38] propose an immersed boundary condition through implicitly incorporating the boundary conditions with the differential-algebraic equations using a half-explicit Runge-Kutta method. Subsequently, Ménez et al. [39] propose a sharp interface method by combining the advantages of the ghost cell IBMs and the volume penalization method. Moreover, Ménez et al. [39] compare the numerical results generated by the traditional feedback forcing IBM with those of the sharp interface method and the body-fitted method, where they find that the feedback forcing IBM cannot accurately enforce the boundary conditions on the immersed surface and the pressure field is polluted by the diffusion effects induced by the regularization delta function. In addition, Ménez et al. [39] point out that the difference in predicted results between the existing diffuse interface IBMs and body-fitted methods is relatively significant. Note that although Wang et al. [35] and Ménez et al. [39] have successfully implemented the feedback forcing IBM in a compressible flow environment, there are several artificial parameters in the feedback forcing IBM, such as the arbitrary parameters for calculating IBM forcing terms, that need to be defined through extensive numerical tests.

In this work, a novel one-side diffuse-interface IBM for compressible flows is proposed within the framework of the continuous forcing IBM, where the boundary conditions in conventional body-fitted methods and sharp interface approaches are accurately satisfied by the proposed diffuse IBM, such as the pressure boundary condition, the isothermal and heat-flux boundary conditions. The differences between the desired boundary values and the intermediate flow field are implicitly calculated by solving linear systems, and then these differences are adopted as Lagrangian corrections at boundary points. Moreover, this new IBM adopts a novel spreading scheme to suppress the diffusion effects introduced by the regularization delta function, where the Lagrangian corrections are biasedly distributed to the Eulerian points inside the solid body. By constructing linear systems to guarantee the equality between the interpolation and the spreading processes, this novel IBM can precisely implement boundary conditions on the solid surface and the boundary condition discretization errors are negligible.

The remainder of the paper is organized as follows. The governing equations and the numerical method for compressible viscous flows are presented in Section 2. In Section 3, the methodology of the proposed one-side diffuse-interface IBM is presented. In Section 4, the numerical accuracy test and numerical validations of the proposed diffuse IBM are conducted. Conclusions are provided in Section 5.

2. The governing equations and numerical methods

In this section, the governing equations of compressible viscous flows are introduced, in which the Navier-Stokes equations are decoupled into the prediction and correction steps through applying a fractional step method. In the prediction step, the compressible viscous flow is simulated by the gas kinetic flux solver (GKFS), where the boundary effects of the immersed object are neglected. Subsequently, in the correction step, the predicted flow field is corrected by the proposed diffuse interface IBM for accurately enforcing the Dirichlet and Neumann boundary conditions on the immersed boundary.

2.1. Compressible Navier-Stokes (N-S) equations

The macroscopic governing equations for compressible viscous flows can be derived by the mass, momentum and energy conservation laws, which can be written as:

$$\frac{\partial \mathbf{W}}{\partial t} + \nabla \cdot \mathbf{F} = \mathbf{f}, \tag{1a}$$

$$\mathbf{W} = \begin{Bmatrix} \rho \\ \rho \mathbf{u} \\ \rho E \end{Bmatrix}, \quad \mathbf{F} = \begin{Bmatrix} \rho \mathbf{u} \\ \rho \mathbf{u} \otimes \mathbf{u} + p\boldsymbol{I} - \boldsymbol{\Pi} \\ (\rho E + p)\mathbf{u} - \kappa \nabla T - \mathbf{u} \cdot \boldsymbol{\Pi} \end{Bmatrix}, \tag{1b}$$

$$\boldsymbol{\Pi} = \mu \left[\left(\nabla \mathbf{u} + (\nabla \mathbf{u})^{\mathrm{T}} \right) - \frac{2}{3} (\nabla \cdot \mathbf{u}) \boldsymbol{I} \right], \tag{1c}$$

where ρ, $\mathbf{u}$, p, E, κ and μ represent the flow density, the velocity, the pressure, the total energy, the thermal conductivity and the dynamic viscosity, respectively. In this study, the internal relationship between the density ρ, the pressure p and the temperature T is described by the state equation for ideal gas as $p = \rho RT$, where R is the specific gas constant. The dynamic viscosity μ is derived by the Sutherland's law. The thermal conductivity is defined as $\kappa = C_p \mu / Pr$, in which C_p denotes the specific heat coefficient at constant pressure and is defined as $C_p = \gamma R/(\gamma - 1)$. In addition, Pr and γ are the Prandtl number and the specific heat ratio, respectively. The right hand term of the governing equation (1a) denotes the IBM volume forces $\mathbf{f} = \left(\mathrm{f}_\rho, \mathbf{f}_\mathbf{u}, \mathrm{f}_\mathrm{E} \right)^{\mathrm{T}}$.

2.2. The solution process of N-S equations

Based on the fractional step method, the process of solving N-S equations can be decomposed into the prediction and correction steps as

$$\frac{\mathbf{W}_i^* - \mathbf{W}_i^n}{\Delta t} + \frac{1}{\Omega_i} \sum_{j \in N(i)} \boldsymbol{n}_{ij} \cdot \mathbf{F}_{ij} S_{ij} = 0, \quad \text{prediction step}, \tag{2a}$$

$$\frac{\mathbf{W}_i^{n+1} - \mathbf{W}_i^*}{\Delta t} = \mathbf{f}_i, \quad \text{correction step}, \tag{2b}$$

where Ω_i and N_i denote the volume and the number of interface of the ith control volume, respectively. In addition, $\boldsymbol{n}_{ij}$, $\mathbf{F}_{ij}$ and S_{ij} are the normal vector, the flux vector and the area of the jth cell interface. Note that the superscripts n, $*$ and $n+1$ represent the current, the intermediate and the next time steps, respectively. In the prediction step, the flow field is predicted by the flow solver without considering the effects of IBM volume forces, where f_ρ, $\mathbf{f}_\mathbf{u}$ and f_E are set as zero. The N-S equations are solved by a finite volume method, in which the GKFS is adopted to calculate the viscous and inviscid fluxes on the interfaces between two adjacent cells. Thereby, the intermediate density ρ^*, the intermediate flow velocity $\mathbf{u}^*$, and the intermediate total energy E^* are predicted. Subsequently, the IBM is employed to distribute the volume forces at Lagrangian points to the background Eulerian grids, where the IBM volume forces are evaluated though the difference between the intermediate flow field and the desired boundary conditions. Consequently, the flow field is updated to the next time step $n+1$ with boundary conditions being accurately enforced.

2.3. The GKFS for predicting the intermediate flow variables

In the prediction step, the intermediate flow variables $\mathbf{W}^*$ are predicted by the GKFS which has the second order of accuracy in space. Within the framework of a cell-centered finite volume method, the GKFS is employed to calculate the numerical flux $\mathbf{F}_n$ at all cell interfaces of the control volume. The flux vector at a cell interface can be calculated by the local distribution function f though the following relationship

$$\mathbf{F}_n = \int \mathrm{u}_n \boldsymbol{\Phi} f \left(\mathbf{x}_{ij}, \mathbf{u}_p, \boldsymbol{\xi}, t + \delta t \right) d\Xi, \tag{3}$$

where $\mathbf{u}_p = (u_p, v_p)$ denotes the transnational velocity of particle and u_n is the normal component of particle velocity. $\boldsymbol{\xi} = (\xi_1, \xi_2, \cdots, \xi_K)$ is the internal variable, where K denotes the total number of degrees of freedom and is defined as $K = 2/(\gamma - 1) - 2$ in two dimensions. $\boldsymbol{\Phi}$ represents the vector of moments and $\boldsymbol{\Phi} = \left(1, u_p, v_p, \frac{1}{2} \left(u_p^2 + v_p^2 + \xi^2 \right) \right)^T$, where $\xi^2 = \xi_1^2 + \xi_2^2 + \cdots + \xi_K^2$. δt is the streaming time step. $d\Xi$ represents the volume element in the phase space and is defined as $d\Xi = du_p dv_p d\xi_1 d\xi_2 \cdots d\xi_K$.

According to the Chapman-Enskog analysis, to recover N-S equations, the distribution function f can be approximately evaluated through

$$f = \mathrm{g} - \tau \left(\frac{\partial}{\partial t} + \mathbf{u}_p \cdot \nabla \right) \mathrm{g}, \tag{4}$$

where τ denotes the particle collision time and is defined as $\tau = \mu / p$. g is the Maxwellian equilibrium distribution function and its two-dimensional form can be expressed as

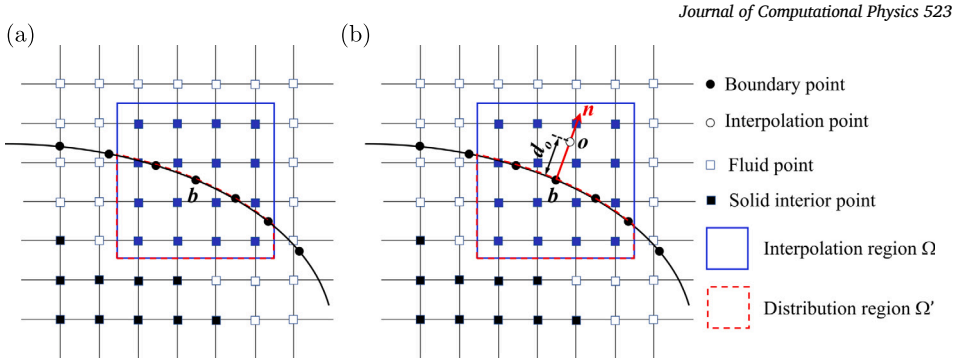

Fig. 1. Illustration of the one-side diffuse-interface IBM for (a) the Dirichlet boundary condition and (b) the Neumann boundary condition, where b denotes the boundary point, o is the interpolation point and d_o is the interpolation distance.

$$\mathrm{g} = \rho\left(\frac{\lambda}{\pi}\right)^{\frac{K+2}{2}} e^{-\lambda\left((u_p-u)^2+(v_p-v)^2+\xi^2\right)}, \tag{5}$$

where u and v denote the macroscopic velocity in the x and y directions, respectively. λ is equal to $\frac{1}{2RT}$. Though implementing the Taylor series expansion in time and physical space, Eq. (4) can be rewritten as

$$\begin{aligned} &f\left(\mathbf{x}_{ij},\mathbf{u}_p,\boldsymbol{\xi},t+\delta t\right)\\ =&\mathrm{g}\left(\mathbf{x}_{ij},\mathbf{u}_p,\boldsymbol{\xi},t+\delta t\right)-\frac{\tau}{\delta t}\left[\mathrm{g}\left(\mathbf{x}_{ij},\mathbf{u}_p,\boldsymbol{\xi},t+\delta t\right)-\mathrm{g}\left(\mathbf{x}_{ij}-\mathbf{u}_p\delta t,\mathbf{u}_p,\boldsymbol{\xi},t\right)\right], \end{aligned} \tag{6}$$

where $\mathrm{g}\left(\mathbf{x}_{ij},\mathbf{u}_p,\boldsymbol{\xi},t+\delta t\right)$ and $\mathrm{g}\left(\mathbf{x}_{ij}-\mathbf{u}_p\delta t,\mathbf{u}_p,\boldsymbol{\xi},t\right)$ represent the Maxwellian equilibrium distribution functions at the cell interface and its surrounding points, respectively. Substituting Eq. (6) into Eq. (3), the numerical flux F_n can be rewritten as

$$\begin{aligned} \mathrm{F}_n=&\int u_n\boldsymbol{\Phi}\left[\mathrm{g}_0-\tau\mathrm{g}_0\left(A_1+A_2u_p+A_3v_p+\frac{1}{2}A_4\left(u_p^2+v_p^2+\xi^2\right)\right)\right]d\boldsymbol{\Xi}\\ &-\tau\left[\frac{\partial}{\partial x}\left(\int_{\mathrm{u}_n\geq 0}\mathrm{u}_nu_p\boldsymbol{\Phi}\mathrm{g}_l d\boldsymbol{\Xi}+\int_{\mathrm{u}_n<0}\mathrm{u}_nu_p\boldsymbol{\Phi}\mathrm{g}_r d\boldsymbol{\Xi}\right)\right.\\ &\left.+\frac{\partial}{\partial y}\left(\int_{\mathrm{u}_n\geq 0}\mathrm{u}_nv_p\boldsymbol{\Phi}\mathrm{g}_l d\Xi+\int_{\mathrm{u}_n<0}\mathrm{u}_nv_p\boldsymbol{\Phi}\mathrm{g}_r d\boldsymbol{\Xi}\right)\right], \end{aligned} \tag{7}$$

where the subscripts "0", "l" and "r" represent the variable at the cell interface, the left side and the right side of the cell interface, respectively. A_1, A_2, A_3 and A_4 are the coefficients. Since the numerical approach for solving compressible viscous flows is not the focus of this study, readers are referred to the previous work [40] for detailed information on the GKFS solver.

3. One-side diffuse-interface IBM for Dirichlet and Neumann boundary conditions

In this section, to eliminate the diffusion effects and the boundary discretization errors in the traditional diffuse IBMs, a novel one-side diffuse-interface IBM is proposed for accurately enforcing the Dirichlet and Neumann boundary conditions, which is inspired by the half distribution forcing strategy proposed in Ji et al. [41]. Shu et al. [42] pointed out that the IBM forcing terms in the governing equations are equivalent to adding corrections to the flow field. Therefore, the IBM volume forces in Eq. (1a) are convert to the flow variable corrections in this work. In the correction step, the IBM is applied to evaluate the difference between the prescribed boundary conditions and the intermediate flow field. Thereafter, the corrected flow variables for the next time step can be calculated by adding the corrected value to the intermediate value as

$$\varphi(\boldsymbol{x},t)=\varphi^*(\boldsymbol{x},t)+\Delta\varphi(\boldsymbol{x},t), \tag{8}$$

where φ denotes the flow variables, such as density, velocity components, pressure and temperature. $\boldsymbol{x}$ denotes the background Eulerian points.

Fig. 1 shows the illustration of this novel one-side diffuse-interface IBM for the Dirichlet and Neumann boundary conditions. The immersed boundary is discretized by a series of Lagrangian points (● in Fig. 1). For the Neumann boundary condition, the interpolation point (○ in Fig. 1) is introduced to evaluate the gradient on the immersed boundary.

3.1. The interpolation and spreading schemes

The intermediate variables at each Lagrangian point $\boldsymbol{X}_b$ can be interpolated as

$$\varphi_b^*(\boldsymbol{X}_b,t)=\int_{\Omega}\varphi^*(\boldsymbol{x},t)\delta_h^b(\boldsymbol{X}_b-\boldsymbol{x})d\boldsymbol{x}, \tag{9}$$

where $d\boldsymbol{x}=dxdy$ represents an Eulerian quadrature. Ω denotes the set of Eulerian points both inside and outside the immersed boundary. δ_h denotes the interpolation kernel, and its 2D form can be expressed as

$$\delta_h(\boldsymbol{X}-\boldsymbol{x})=\frac{1}{h^2}\phi\left(\frac{X-x}{h}\right)\phi\left(\frac{Y-y}{h}\right), \tag{10}$$

where the four-point piecewise function is adopted, which can be written as

$$\phi(r)=\begin{cases}\left[3-2|r|+\sqrt{1+4|r|-4|r|^2}\right]/8, & 0\le|r|<1,\\ \left[5-2|r|-\sqrt{-7+12|r|-4|r|^2}\right]/8, & 1\le|r|<2,\\ 0, & |r|\ge 2.\end{cases} \tag{11}$$

Similarly, the corrections at the Lagrangian points can be interpolated as

$$\Delta\varphi_b(\boldsymbol{X}_b,t)=\int_{\Omega}\Delta\varphi(\boldsymbol{x},t)\delta_h^b(\boldsymbol{X}_b-\boldsymbol{x})d\boldsymbol{x}. \tag{12}$$

To eliminate the diffusion effects introduced by the interpolation kernel, such as the non-physical pressure jump reported in Ménez et al. [39], the Lagrangian corrections are assumed to be distributed to the Eulerian points inside the immersed boundary [41], which can be implemented by the following spreading formulation as

$$\Delta\varphi(\boldsymbol{x},t)=\begin{cases}\int_{\Gamma}\frac{1}{\psi}\Delta\varphi_b(\boldsymbol{X}_b,t)\delta_h^b(\boldsymbol{x}-\boldsymbol{X}_b)\,dS_b, & \text{for } \boldsymbol{x}\in\Omega',\\ 0, & \text{for } \boldsymbol{x}\notin\Omega',\end{cases} \tag{13}$$

where ψ is the scaling factor to guarantee that the flow variable correction at Lagrangian points is fully transferred to surrounding Eulerian points, which is defined as $\psi_i=\sum_{\boldsymbol{x}\in\Omega'}\delta_h^b(\boldsymbol{X}_b^i-\boldsymbol{x})d\boldsymbol{x}$. Ω' denotes the set of Eulerian points only inside the immersed boundary. The flow variable corrections at Eulerian points outside of the immersed boundary are set to zero to retain a sharp fluid–solid interface. Due to the biased distribution of Lagrangian corrections, Eq. (12) can be reduced to

$$\Delta\varphi_b(\boldsymbol{X}_b,t)=\int_{\Omega'}\Delta\varphi(\boldsymbol{x},t)\delta_h^b(\boldsymbol{X}_b-\boldsymbol{x})d\boldsymbol{x}. \tag{14}$$

3.2. The proposed IBM for the Dirichlet boundary condition

For the Dirichlet boundary condition, a implicit system can be established by substituting Eqs. (9), (13) and (14) into Eq. (8) as

$$\begin{aligned}\varphi_b(\boldsymbol{X}_b,t)=&\varphi_b^*(\boldsymbol{X}_b,t)+\int_{\Omega'}\Delta\varphi(\boldsymbol{x},t)\delta_h^b(\boldsymbol{X}_b-\boldsymbol{x})d\boldsymbol{x}\\ =&\varphi_b^*(\boldsymbol{X}_b,t)+\int_{\Omega'}\int_{\Gamma}\frac{1}{\psi}\Delta\varphi_b(\boldsymbol{X}_b,t)\delta_h^b(\boldsymbol{x}-\boldsymbol{X}_b)dS_b\delta_h^b(\boldsymbol{X}_b-\boldsymbol{x})d\boldsymbol{x}.\end{aligned} \tag{15}$$

The above equation can be rewritten in a discretized form as

$$\varphi_b^k(\boldsymbol{X}_b^k,t)=\varphi_b^{*,k}(\boldsymbol{X}_b^k,t)+\sum_{\boldsymbol{x}^j\in\Omega'}\sum_{l=1}^{N_L}\frac{1}{\psi_l}\Delta\varphi_b^l(\boldsymbol{X}_b^l,t)\delta_h^b(\boldsymbol{x}^j-\boldsymbol{X}_b^l)dS_b^l\delta_h^b(\boldsymbol{X}_b^k-\boldsymbol{x}^j)h^2, \tag{16}$$

where N_L is the number of Lagrangian points on the immersed curve boundary Γ. Through solving the above implicit system, the flow variable corrections for satisfying the Dirichlet boundary condition can be accurately evaluated without polluting the external flow field. In this work, for the isothermal solid boundary, the boundary conditions of $u_b=0$, $\partial p/\partial n=0$ and $T_b=T_{ref}$ are enforced.

3.3. The proposed IBM for the Neumann boundary condition

As shown in Fig. 1(b), the discretization form for the general Neumann boundary condition can be expressed as

$$\begin{aligned}\frac{\partial \varphi}{\partial n} &= \frac{\varphi_o - \varphi_b}{d_o} \\ &= \frac{\varphi_o^* + \Delta\varphi_o - \varphi_b^* - \Delta\varphi_b}{d_o},\end{aligned} \tag{17}$$

where the intermediate variables φ_o^* and its corrections $\Delta\varphi_o$ at the interpolation point o can be obtained by

$$\varphi_o^*(\boldsymbol{X}_o, t) = \int_{\Omega} \varphi^*(\boldsymbol{x}, t)\delta_h^o(\boldsymbol{X}_o - \boldsymbol{x})d\boldsymbol{x}, \tag{18}$$

and

$$\Delta\varphi_o(\boldsymbol{X}_o, t) = \int_{\Omega'} \Delta\varphi(\boldsymbol{x}, t)\delta_h^o(\boldsymbol{X}_o - \boldsymbol{x})d\boldsymbol{x}. \tag{19}$$

$\boldsymbol{X}_o$ denotes the physical location of the interpolation point. Substituting Eqs. (9), (13), (14), (18) and (19) into Eq. (17) yields the following relationship

$$\begin{aligned}&\frac{\partial \varphi}{\partial n} d_o - \varphi_o^*(\boldsymbol{X}_o, t) + \varphi_b^*(\boldsymbol{X}_b, t) \\ &= \int_{\Omega'} \Delta\varphi(\boldsymbol{x}, t)\delta_h^o(\boldsymbol{X}_o - \boldsymbol{x})d\boldsymbol{x} - \int_{\Omega'} \Delta\varphi(\boldsymbol{x}, t)\delta_h^b(\boldsymbol{X}_b - \boldsymbol{x})d\boldsymbol{x} \\ &= \int_{\Omega'}\int_{\Gamma} \frac{1}{\psi}\Delta\varphi_b(\boldsymbol{X}_b, t)\delta_h^b(\boldsymbol{x} - \boldsymbol{X}_b)dS_b\delta_h^o(\boldsymbol{X}_o - \boldsymbol{x})d\boldsymbol{x} - \int_{\Omega'}\int_{\Gamma} \frac{1}{\psi}\Delta\varphi_b(\boldsymbol{X}_b, t)\delta_h^b(\boldsymbol{x} - \boldsymbol{X}_b)dS_b\delta_h^b(\boldsymbol{X}_b - \boldsymbol{x})d\boldsymbol{x} \\ &= \int_{\Omega'}\int_{\Gamma} \frac{1}{\psi}\Delta\varphi_b(\boldsymbol{X}_b, t)\delta_h^b(\boldsymbol{x} - \boldsymbol{X}_b)dS_b\left[\delta_h^o(\boldsymbol{X}_o - \boldsymbol{x}) - \delta_h^b(\boldsymbol{X}_b - \boldsymbol{x})\right]d\boldsymbol{x}.\end{aligned} \tag{20}$$

The above equation can be rewritten in a discretized form as

$$\begin{aligned}&\frac{\partial \varphi}{\partial n} d_o - \varphi_o^{*,k}(\boldsymbol{X}_o^k, t) + \varphi_b^{*,k}(\boldsymbol{X}_b^k, t) \\ &= \sum_{\boldsymbol{x}^j \in \Omega'}\sum_{l=1}^{N_L} \frac{1}{\psi_l}\Delta\varphi_b^l(\boldsymbol{X}_b^l, t)\delta_h^b(\boldsymbol{x}^j - \boldsymbol{X}_b^l)dS_b^l\left[\delta_h^o(\boldsymbol{X}_o^k - \boldsymbol{x}^j) - \delta_h^b(\boldsymbol{X}_b^k - \boldsymbol{x}^j)\right]h^2.\end{aligned} \tag{21}$$

The corrections for satisfying the Neumann boundary condition can be calculated by solving the above implicit system. Meanwhile, these corrections guarantee that the diffusion effects will not be propagated to the external flow field. To be consistent with the gradient calculated from the background flow field, the interpolation distance is set to $d_o = h$. In this work, for the adiabatic solid wall, the boundary conditions of $u_b = 0$, $\partial p/\partial n = 0$ and $\partial \rho/\partial n = 0$ are enforced following the previous studies [43,44]. Note that the generalized minimum residual algorithm is adopted to solve the sparse linear systems in Eqs. (16) and (21), where the compressed row technique is employed to reduce the memory space.

In the present work, the aerodynamic forces on the immersed object can be directly evaluated through the volume integration of momentum correction as:

$$\boldsymbol{F}_f = -\sum_{i=1}^{N_E} \frac{\Delta(\rho\mathbf{u})}{\Delta t}h^2 = -\sum_{i=1}^{N_E} \frac{\left(\rho^{n+1}\mathbf{u}^{n+1} - \rho^*\mathbf{u}^*\right)}{\Delta t}h^2, \tag{22}$$

where N_E denotes the number of affected Eulerian points.

3.4. Computational sequence

The overall computational sequences for enforcing the isothermal and adiabatic boundary conditions by the proposed one-side diffuse-interface IBM are shown in **Algorithm 1** and **Algorithm 2**, respectively. Note that the procedure for implementing the no-slip boundary condition follows the previous work [16] and is not presented in these two algorithms.

3.5. Comparison with the conventional one-side IBM and existing diffuse interface IBMs for compressible flows

3.5.1. The conventional one-side IBM for the Dirichlet boundary condition

In this section, the conventional iterative one-side IBM proposed by Ji et al. [41] is briefly introduced.

Algorithm 1 Method for enforcing the isothermal boundary condition

1: Predict the intermediate flow variables p^* and T^*;
2: Calculate the Lagrangian corrections for the isothermal boundary condition in Eq. (16);
3: Calculate the Lagrangian corrections for the pressure boundary condition in Eq. (21);
4: Spread the Lagrangian corrections to the surrounding Eulerian points using Eq. (13);
5: Calculate the updated pressure $p^{n+1} = p^* + \Delta p$ and temperature $T^{n+1} = T^* + \Delta T$;
6: Calculate the updated density through $\rho^{n+1} = p^{n+1}/RT^{n+1}$.

Algorithm 2 Method for enforcing the adiabatic boundary condition

1: Predict the intermediate flow variables p^* and T^*;
2: Calculate the Lagrangian corrections for the density boundary condition in Eq. (21);
3: Calculate the Lagrangian corrections for the pressure boundary condition in Eq. (21);
4: Spread the Lagrangian corrections to the surrounding Eulerian points using Eq. (13);
5: Calculate the updated pressure $p^{n+1} = p^* + \Delta p$ and density $\rho^{n+1} = \rho^* + \Delta\rho$;
6: Calculate the updated temperature through $T^{n+1} = p^{n+1}/R\rho^{n+1}$.

(1) Initialize the iteration number $k = 0$ and $\varphi^{*(0)}(\boldsymbol{x}, t) = \varphi^*(\boldsymbol{x}, t)$.
(2) Interpolate the intermediate flow variables at Lagrangian points $\varphi_b^{*(k)}(\boldsymbol{X}_b, t)$ by using Eq. (9).
(3) Calculate the variable corrections at Lagrangian points as

$$\Delta\varphi_b^{(k)}(\boldsymbol{X}_b, t) = \varphi_b(\boldsymbol{X}_b, t) - \varphi_b^{*(k)}(\boldsymbol{X}_b, t). \tag{23}$$

(3) Spread the Lagrangian variable corrections to the surrounding Eulerian points as

$$\Delta\varphi^{(k)}(\boldsymbol{x}, t) = \int_\Gamma \frac{1}{\psi}\Delta\varphi_b^{(k)}(\boldsymbol{X}_b, t)\delta_h^b(\boldsymbol{x} - \boldsymbol{X}_b)dS_b, \quad \boldsymbol{x} \in \Omega'. \tag{24}$$

(4) Update the flow variable as

$$\varphi^{*(k+1)}(\boldsymbol{x}, t) = \varphi^{*(k)}(\boldsymbol{x}, t) + \Delta\varphi^{(k)}(\boldsymbol{x}, t). \tag{25}$$

(5) Repeat steps 2-4 until achieving the maximum iteration number.

Note that the maximum iteration number in Ji et al. [41] is artificially determined; thus, the iterative one-side IBM cannot achieve a certain convergence rate and maintain the boundary errors of the Dirichlet boundary condition within a specific accuracy criterion.

3.5.2. The feedback forcing IBM

In this section, the methodology of the feedback forcing IBM for implementing the Dirichlet and Neumann boundary conditions are presented. For the no-slip boundary condition, the flow velocity components at Lagrangian points are interpolated by Eq. (9), and then the momentum forcing terms at Lagrangian points can be explicitly defined as:

$$\mathbf{F}_u(\boldsymbol{X}_b, t) = \alpha \int_0^t \left(\mathbf{u}_b - \mathbf{u}^*\left(\boldsymbol{X}_b, t'\right)\right) dt' + \beta\left(\mathbf{u}_b - \mathbf{u}^*(\boldsymbol{X}_b, t)\right), \tag{26}$$

where α and β are arbitrary parameters. Subsequently, the momentum forcing terms at Lagrangian point are spread on the Eulerian grids through

$$\mathbf{f}_u(\boldsymbol{x}, t) = \rho(\boldsymbol{x}, t)\int_\Gamma \mathbf{F}_u(\boldsymbol{X}_b, t)\delta_h^b(\boldsymbol{x} - \boldsymbol{X}_b)dS_b. \tag{27}$$

For the isothermal boundary condition, the effects of solid boundary are converted to the energy forcing term f_E in Eq. (1a). At Lagrangian points, the total energy can be calculated through the stiffened gas equation of state as

$$E_b(\boldsymbol{X}_b, t) = \frac{1}{2}\mathbf{u}_b^2 + c_v T_b + \frac{P_\infty}{\rho(\boldsymbol{X}_b, t)}. \tag{28}$$

The intermediate total energy at Lagrangian points can be interpolated by Eq. (9). Similarly, the energy forcing term at Lagrangian points can be derived as

$$F_E(\boldsymbol{X}_b, t) = \alpha \int_0^t \left(E_b\left(\boldsymbol{X}_b, t'\right) - E^*\left(\boldsymbol{X}_b, t'\right)\right) dt' + \beta\left(E_b\left(\boldsymbol{X}_b, t\right) - E^*\left(\boldsymbol{X}_b, t\right)\right). \tag{29}$$

Thereafter, the energy forcing term at Lagrangian point is distributed on the Eulerian grids through

$$f_E(\boldsymbol{x}, t) = \rho(\boldsymbol{x}, t)\int_\Gamma F_E(\boldsymbol{X}_b, t)\delta_h^b(\boldsymbol{x} - \boldsymbol{X}_b)dS_b. \tag{30}$$

For the adiabatic boundary condition, the boundary temperature can be approximately evaluated as

$$T_b(\boldsymbol{X}_b,t)=T_o(\boldsymbol{X}_o,t)=\int_{\Omega}T(\boldsymbol{x},t)\delta_h^o(\boldsymbol{X}_o-\boldsymbol{x})d\boldsymbol{x}. \tag{31}$$

Based on the methodology of the feedback forcing IBM, the boundary errors are significantly affected by the artificial parameters α and β. In addition, the inequality between the interpolation and spreading processes is not taken into consideration. In the feedback forcing IBM, the IBM forces at Lagrangian points are spread on the double side of the solid boundary. Therefore, the numerical results predicted by the feedback forcing IBM deviate from the body-fitted results and the non-physical pressure jump occurs before the stagnation point [39]. For compressible flows, Ménez et al. [39] only enforce the no-slip and thermal boundary conditions, while the pressure boundary condition is neglected, indicating that the traction continuity at the solid–fluid interface may not be satisfied.

3.5.3. The velocity-correction IBM with iterative density correction

In this section, the methodology of the velocity-correction IBM with iterative density correction is presented. Similarly, the velocity-correction IBM constructs a linear system similar to Eq. (16) to solve the velocity and temperature corrections for satisfying the no-slip and isothermal boundary conditions. Then, the continuity equation can be rewritten as

$$\frac{\partial(\rho^*+\Delta\rho)}{\partial t}+\frac{\partial(\rho^*+\Delta\rho)(u^*+\Delta u)}{\partial x}+\frac{\partial(\rho^*+\Delta\rho)(v^*+\Delta v)}{\partial y}=0. \tag{32}$$

The density correction can be evaluated through a iterative process as

$$\left(\Delta\rho^{k+1}\right)_{i,j}=-\Delta t\left[\frac{\left(u^{n+1}\Delta\rho^k\right)_{i+1,j}-\left(u^{n+1}\Delta\rho^k\right)_{i-1,j}}{2h}+\frac{\left(v^{n+1}\Delta\rho^k\right)_{i,j+1}-\left(v^{n+1}\Delta\rho^k\right)_{i,j-1}}{2h}+S_{i,j}\right]. \tag{33}$$

Once the density and temperature corrections are obtained, the pressure can be updated by the equation of state as $p^{n+1}=(\rho^*+\Delta\rho)R(T^*+\Delta T)$. However, when solving the density correction, the iterative process is performed both inside and outside of the solid boundary, which will induce the mass exchange across the immersed boundary. Moreover, the velocity-correction IBM with iterative density correction can only enforce the Dirichlet boundary condition. Note that the pressure boundary condition is also not taken into consideration in this IBM. Consequently, the density, pressure and velocity contours show significant difference with body-fitted results [36], and the pressure distribution on the solid boundary deviates from the body-fitted results [34,36].

In contrast to the aforementioned diffuse interface IBMs, the advantages of the proposed one-side diffuse interface IBM can be concluded as

- With respect to the conventional iterative one-side IBM [41], the proposed one-side diffuse interface IBM is fully implicit and can accurately enforce the Dirichlet boundary condition. The proposed IBM can maintain the boundary errors at the level of machine round-off by solving a linear system.
- The proposed IBM extends the one-side spreading scheme with the implicit scheme to enforce the Neumann boundary condition, which guarantees that the boundary errors of the Neumann boundary condition are close to machine accuracy.
- The one-side diffuse interface IBM is firstly extended to compressible flows, where the one-side spreading scheme can retain a sharp fluid-solid interface to suppress the non-physical pressure jump in the traditional diffuse IBM [39].
- With respect to the feedback forcing IBM [35,39], the present IBM does not need to introduce artificial parameters to calculate the restoring force terms.
- With respect to the feedback forcing IBM [39] and the velocity-correction IBM with iterative density correction [36], the no-slip, pressure, isothermal and adiabatic boundary conditions are implicitly enforced by the present IBM with negligible boundary errors.

4. Results and discussions

In this section, the numerical accuracy of the proposed one-side diffuse-interface IBM integrated with the GKFS is tested. Subsequently, the supersonic flows past a circular cylinder with the isothermal and adiabatic wall boundary conditions are adopted to examine the accuracy and capability of the proposed diffuse interface IBM. In addition, the proposed diffuse interface IBM is extended to simulate supersonic flows around complex geometries, such as an elliptical cylinder, 5-point stars and the Apollo Command Module, which further demonstrate the accuracy and flexibility of the proposed diffuse interface IBM for complex geometries.

4.1. Overall accuracy test

In this subsection, the supersonic flow past an adiabatic circular cylinder is adopted to examine the overall accuracy of the proposed IBM for compressible flows. The parameters in this test are $Ma_\infty=u_\infty/c_\infty=2.0$ and $Re_\infty=\rho_\infty u_\infty D/\mu=300$, where u_∞, c_∞, ρ_∞ and D denote the free-stream velocity, sound speed, density and the diameter of the circular cylinder, respectively. The pressure coefficient is defined as $C_p=(p-p_\infty)/(0.5\rho_\infty u_\infty^2)$. The circular cylinder is located at the origin and the size of the numerical domain is $[-15D,25D]\times[-15D,15D]$, in which the uniform mesh is employed to discretize the sub-region around the cylinder $[-0.6D,0.6D]\times[-0.6D,0.6D]$. The numerical accuracy tests are conducted on five different meshes, where the sub-region is uniformly

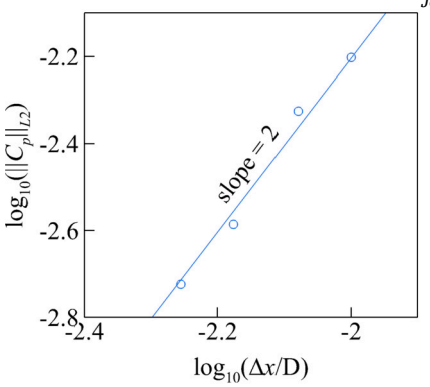

Fig. 2. Convergence of numerical error versus mesh spacing for supersonic flow past an adiabatic circular cylinder.

discretized with five mesh spacings, namely, $D/100$, $D/120$, $D/150$, $D/180$ and $D/200$. The ratio between the Lagrangian point spacing and the background mesh spacing is fixed as $\pi/2$. The predicted results generated by the finest mesh ($D/200$) are employed as the reference solution. The relative error of pressure coefficient $\left\|C_p\right\|_{L_2}$ is evaluated at dimensionless time $t^* = tu_\infty/D = 100$ and defined as

$$\left\|C_p\right\|_{L_2} = \sqrt{\frac{\sum_{i=1}^{N_L}\left\|(C_p)_i^{numerical} - (C_p)_i^{reference}\right\|^2}{\sum_{i=1}^{N_L}\left\|(C_p)_i^{reference}\right\|^2}}, \tag{34}$$

where the reference pressure is interpolated from the pressure field generated by the finest mesh ($h = D/200$) at the same location.

As shown in Fig. 2, the overall accuracy of the proposed IBM integrated with the GKFS for compressible flows is second-order in space, indicating that the proposed IBM does not affect the global accuracy of the GKFS. Note that the overall accuracy of the present diffuse interface IBM is higher than the traditional diffuse interface IBM [39], it may be that the inequality between the interpolations and the spreading processes is eliminated; thereby, the discretization errors induced by the proposed IBM are negligible.

4.2. Supersonic flow past an isothermal circular cylinder

In this subsection, supersonic flow past an isothermal circular cylinder is adopted to examine the accuracy and ability of the proposed IBM for compressible flow. This numerical test is governed by the following dimensionless parameters: $Ma_\infty = 2$ and $Re_\infty = 300$. The free-stream temperature is set to $T_\infty = 162.8K$, indicating that the stagnation temperature is $T_s = 293K$. In this test, the wall temperature is set as $T_{ref} = 2T_s = 586K$. The domain size of this problem is the same as Section 4.1, where the region of $[-1.5D, 1.5D]\times[-1.5D, 1.5D]$ is uniformly discretized with the mesh spacing of $D/200$ to accurately capture the shock interface. To examine whether the boundary conditions are accurately satisfied, the instantaneous boundary errors are presented in Fig. 3, where the isothermal boundary error is defined as $\left|T_w - T_{ref}\right|/T_\infty$ and the pressure boundary error is defined as $\left|\left(\frac{\partial p}{\partial n}\right)_w - \left(\frac{\partial p}{\partial n}\right)_{ref}\right|$. The subscript "$w$" denotes the flow variables interpolated from the corrected flow field at Lagrangian points. As shown in Figs. 3(b) and 3(c), the boundary errors are extremely small and close to the machine accuracy, indicating that the Dirichlet and Neumann boundary conditions are accurately enforced at the Lagrangian points, and the boundary errors show negligible effects on the overall accuracy. In addition, the boundary errors generated by using the conventional iterative one-side IBM [41] with 10 inner iterations are also presented in Fig. 3(a), where the boundary errors for the Dirichlet boundary condition are noticeable, indicating that the isothermal boundary condition is not accurately enforced.

Fig. 4 shows the pressure profile along the stagnation line, where the numerical results predicted by the proposed IBM are compared with those of the body-fitted method, the sharp interface method and the diffuse interface IBM in Ménez et al. [39]. It is evident from Fig. 4 that the numerical results generated by the proposed IBM agree well with those of the body-fitted method and the sharp interface method. It is noteworthy that the non-physical pressure drop right before the stagnation point in the previous diffuse IBM is eliminated in the present diffuse IBM, because the Lagrangian corrections are only distributed on the fluid points inside the solid body and the regularization delta function's diffusion effects do not pollute the flow field outside the immersed object.

In addition, the temperature profile along the stagnation line and the pressure distribution on the circular cylinder's surface generated by the proposed IBM are compared with the previous study [39] in Fig. 5. It can be seen that the temperature profile predicted by the proposed diffuse interface IBM agree well with those of the body-fitted method and the sharp interface method, where the position of the shock (temperature jump's position) is consistent with the previous body-fitted results. Moreover, it is evident from Fig. 5(b) that the proposed diffuse interface IBM can predict correct pressure distribution on the cylinder's surface, while the numerical results of the previous diffuse interface IBM show notably discrepancies with the body-fitted results [39].

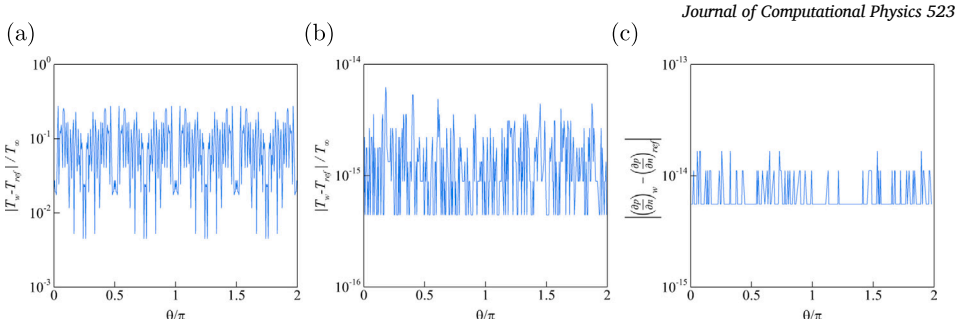

Fig. 3. Boundary errors for the Dirichlet boundary condition by using (a) the iterative one side IBM proposed by Ji et al. [41] and (b) the present IBM. (c) Boundary errors for the Neumann boundary condition by using the present IBM.

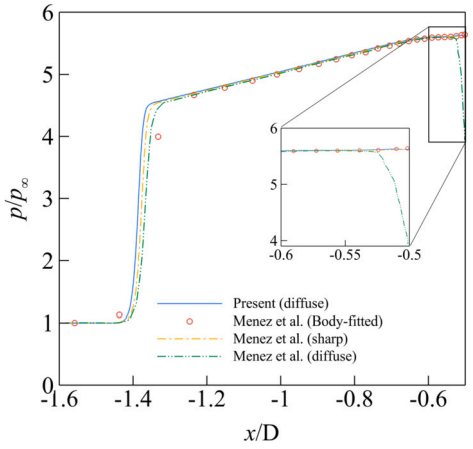

Fig. 4. Pressure profile along the stagnation line ($y/D = 0$) of supersonic flow past an isothermal circular cylinder ($Ma_\infty = 2$, $Re_\infty = 300$ and $T_{ref} = 2T_s$), where the stagnation point is located at $x/D = -0.5$.

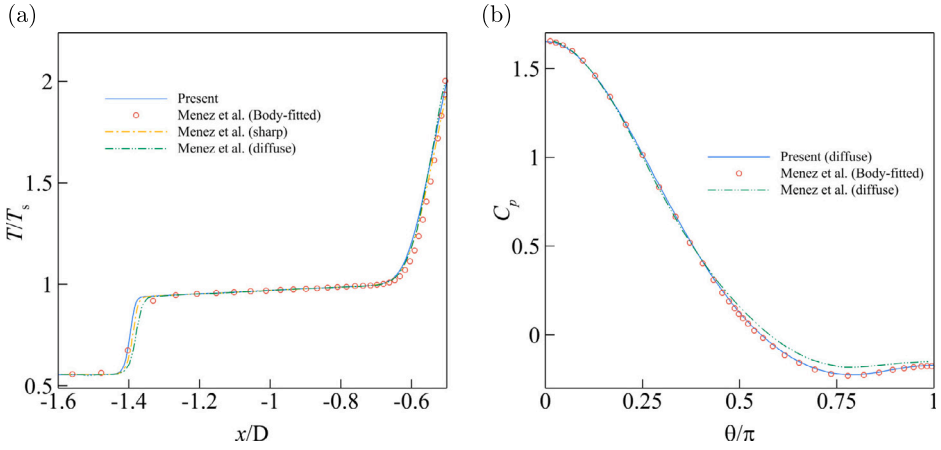

Fig. 5. (a) Temperature profile along the stagnation line ($y = 0$) of supersonic flow past an isothermal circular cylinder ($Ma_\infty = 2$, $Re_\infty = 300$ and $T_{ref} = 2T_s$); (b) pressure distribution on the heated cylinder's surface.

4.3. Supersonic flow past an adiabatic circular cylinder

In this subsection, the supersonic flow past an adiabatic circular cylinder is numerical investigated to further verify the suitability and accuracy of the proposed IBM for simulating compressible flows. The computational domain configuration is the same as that in Section. 4.2. The parameters in this problem are set as: $Ma_\infty = 1.2$ and 2, $Re_\infty = 300$. Fig. 6 presents the comparisons of the pressure, u-velocity, and v-velocity contours between the reference contours of Sun et al. [36] and the present results. As shown in Fig. 6, the results obtained by the proposed diffuse interface IBM agree well with the body-fitted results (left column: background

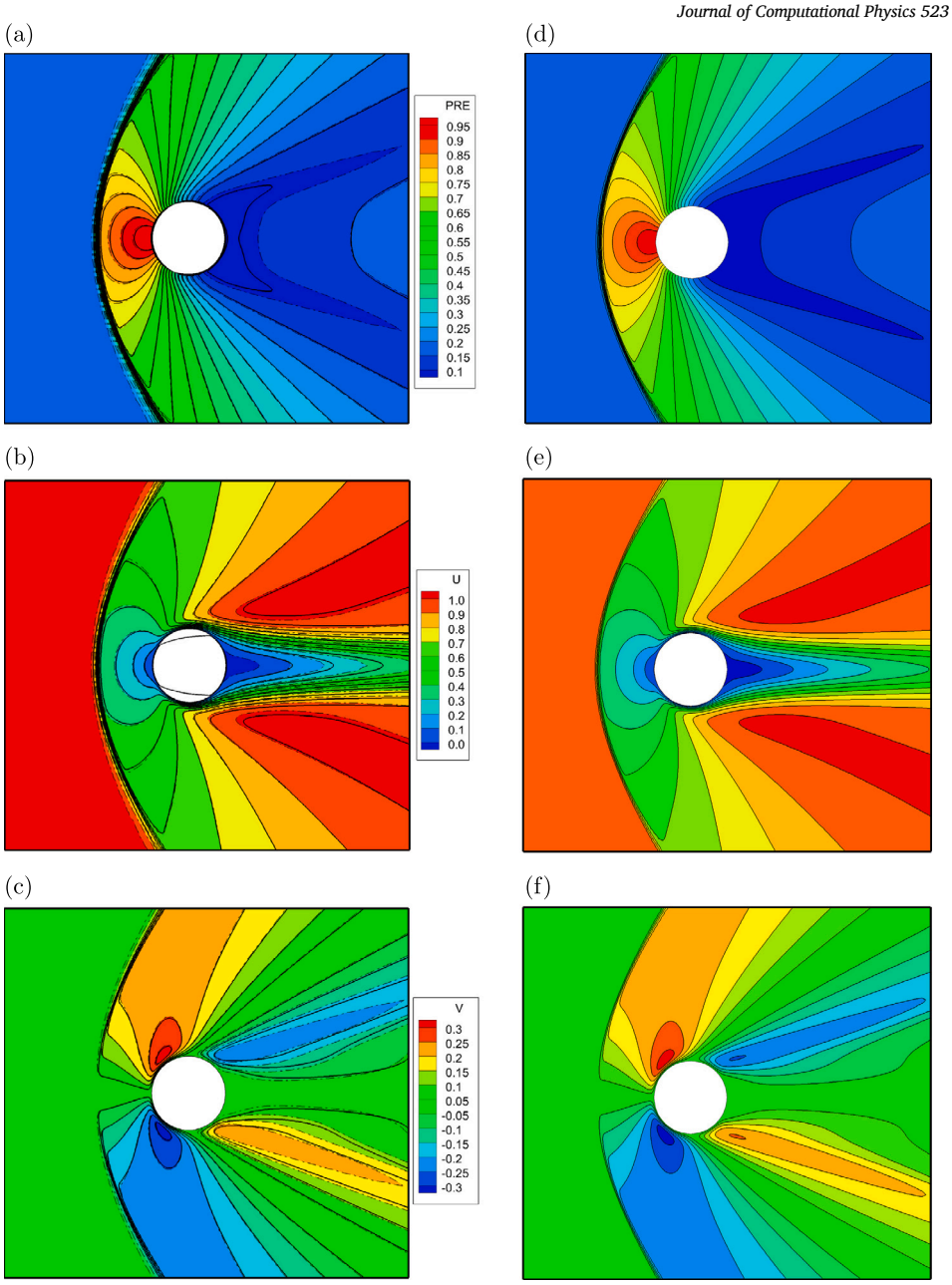

Fig. 6. Comparisons of pressure contours (first row), u-velocity contours and v-velocity contours of supersonic flow past an adiabatic circular cylinder ($Ma_\infty = 2$ and $Re_\infty = 300$). Left column: reference contours of Sun et al. [36], where background contours with dash lines are generated by the body-fitted method [45] and the contours with solid lines are predicted by the previous diffuse IBM proposed by Sun et al. [36]; right column: present results.

contours with dash lines). In contrast, the results predicted by the previous diffuse interface IBM [36] have significant discrepancies with the body-fitted results, indicating that the present diffuse interface IBM has successfully enforced the boundary conditions on the immersed object. Especially, the wake recirculation phenomenon is not captured by the previous diffuse interface IBM [36] and is accurately predicted by the proposed diffuse interface IBM, which qualitatively demonstrates that the predicted results of the present IBM are more consistent with the body-fitted results. Note that the pressure distribution in the wake region has a slight deviation with the body-fitted results, which may be caused by different mesh configurations adopted in the respective simulations.

To quantitatively examine the accuracy and capability of the proposed diffuse interface IBM for compressible flows, the pressure profile along the stagnation line is presented in Fig. 7. It is evident from Fig. 7 that the predicted pressure profile is in a good agreement with the results of the body-fitted method and the sharp interface method, indicating that the proposed diffuse interface IBM has accurately captured the shockwave position. Moreover, the non-physical pressure jump by the previous diffuse interface IBM reported in Ref. [39] is completely eliminated, which means that the present diffuse interface IBM can accurately predict the characteristics of

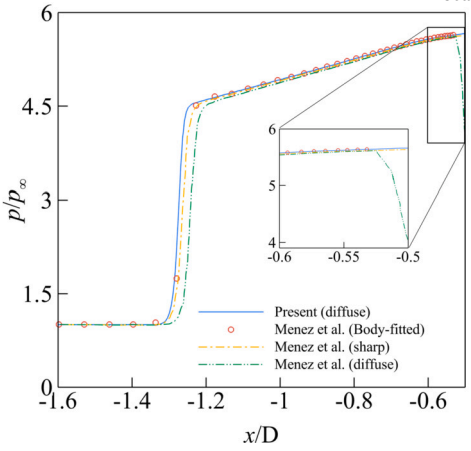

Fig. 7. Pressure profile along the stagnation line ($y/D = 0$) for the supersonic flow past an adiabatic circular cylinder at $Ma_\infty = 2$ and $Re_\infty = 300$.

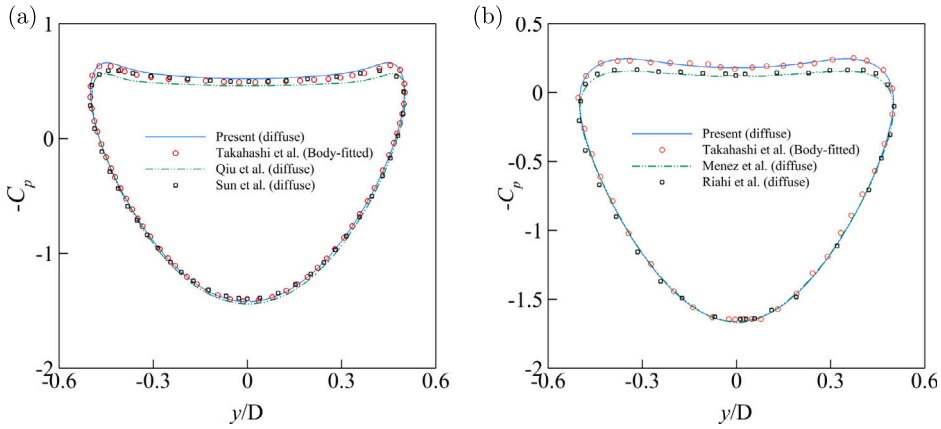

Fig. 8. Pressure distribution on the adiabatic cylinder's surface at (a) $Ma_\infty = 1.2$ and (b) $Ma_\infty = 2.0$.

Table 1
Comparison of drag coefficient C_d and shock stand-off distance Δs for the supersonic flow past an adiabatic circular cylinder at $Ma_\infty = 2.0$ and $Re_\infty = 300$.

Reference	C_d	Δs
Takahashi et al. [46], body-fitted	1.55	-
Riahi et al. [37], diffuse	1.51	0.69
Ménez et al. [39], diffuse	1.59	0.73
Ménez et al. [39], body-fitted	1.62	0.73
Ménez et al. [39], sharp	1.60	0.72
Present, diffuse	1.62	0.75

compressible flows without diffusion effects. In addition, the pressure distributions on the circular cylinder's surface at $Ma_\infty = 1.2$ and 2 are compared with the previous studies [34,36,37,39,46] in Fig. 8. It can be seen that the numerical results predicted by the proposed diffuse interface IBM are in a good agreement with the body-fitted results at different Mach numbers. In contrast, the previous diffuse interface IBMs' results cannot match well with the body-fitted results, especially on the leeward side [34,36,37,39]. Ménez et al. [39] pointed out that the previous diffuse interface IBM cannot accurately predict the downstream pressure. Surprisingly, the proposed diffuse IBM can accurately generate the downstream pressure, because the pressure and temperature boundary conditions are precisely enforced by the proposed diffuse interface IBM without polluting the flow field outside the solid object. To further evaluate the accuracy of the proposed diffuse interface IBM, Table 1 compares the drag coefficient C_d and the shock stand-off distance Δs with those of previous studies [37,39,46]. It is evident from Table 1 that the predicted results are in a good agreement with the reference data, which further confirms the suitability of the proposed diffuse interface IBM for simulating compressible flows.

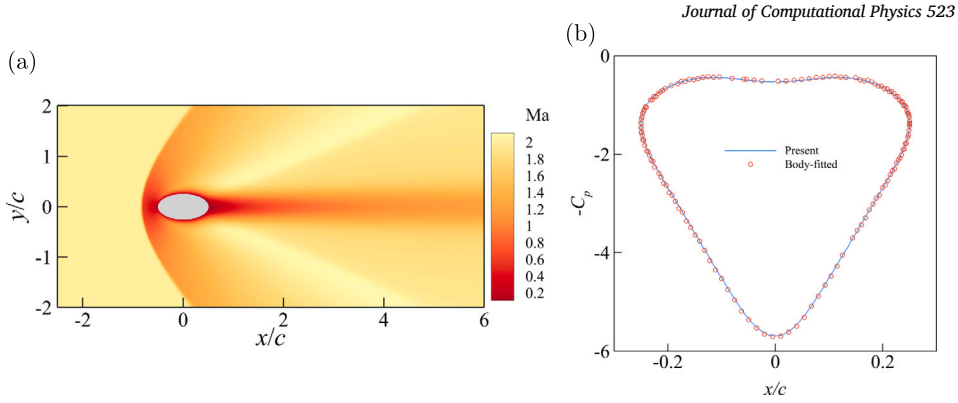

Fig. 9. (a) The Mach contours of compressible flows past an adiabatic ellipse cylinder at $Ma_\infty = 2.0$ and $Re_\infty = 300$; (b) the pressure distribution on the ellipse cylinder's surface.

4.4. Supersonic flow past a bluff body with complex geometries

Previous sections present the ability of the proposed diffuse interface IBM for simulating compressible flows past a circular cylinder with different thermal boundary conditions. In this subsection, simulations of compressible flows past solid objects with complex geometries are conducted to examine the capability of the proposed IBM. Firstly, the compressible flow past an adiabatic ellipse cylinder is simulated. The ellipse with a thickness e to chord length c ratio ($\epsilon = e/c$) of $1/2$, and the dimensionless flow parameters are $Ma_\infty = 2.0$ and $Re_\infty = \rho_\infty u_\infty c/\mu = 300$. Similar to the compressible flow past a circular cylinder, the flow configurations present a detached bow shock at the upstream of the cylinder and a steady downstream wake (see Fig. 9(a)). Besides, the shockwave position is closer to the solid object than the circular cylinder configuration.

To quantitatively verify the accuracy of the proposed diffuse interface IBM for irregular geometries, the pressure distribution on the ellipse cylinder's surface is presented in Fig. 9(b). To our knowledge, there is no reference case of the compressible past an adiabatic ellipse, so the results are compared to the body-fitted results. It can be seen that the present results are in a good agreement with the body-fitted results, indicating the flow characteristics around the immersed object are accurately predicted. Moreover, the pressure and temperature profiles along the stagnation line ($y/c = 0$) and the upward line ($y/c = 0.3$) are presented in Fig. 10. It is evident from Fig. 10 that good agreements between present results and body-fitted results are achieved, where the shockwave position, the pressure and temperature jumps agree well with the body-fitted results. These numerical observations demonstrate that the proposed diffuse interface IBM can accurately simulate the compressible flows past solid body with irregular geometries.

To further test the ability of the proposed diffuse interface IBM for simulating supersonic flow past solid objects with complex geometries, two adiabatic 5-point stars are adopted in this subsection. The geometry of the 5-point star is defined by the following equation as:

$$\begin{pmatrix} X_b \\ Y_b \end{pmatrix} = \begin{pmatrix} \left[r_0 + \Delta r \cos(5\theta)\right]\cos(\theta) \\ \left[r_0 + \Delta r \cos(5\theta)\right]\sin(\theta) \end{pmatrix}, \tag{35}$$

where r_0 and Δr denote the averaged radius and the maximum radial perturbation, respectively. In this problem, the geometry parameters are set as: $r_0 = 0.5$, $\Delta r = 0.05$ and 0.1; the corresponding geometries are shown in Fig. 11. The dimensionless flow parameters are: $Ma_\infty = 2.0$ and $Re_\infty = \rho_\infty u_\infty 2r_0/\mu = 200$.

Figs. 12 and 13 show the pressure and temperature profiles along the stagnation line and the upward line at $\Delta r = 0.05$ and 0.1, respectively. It can be seen that the pressure and temperature distributions are consistent with body-fitted results, indicating that the proposed diffuse interface IBM accurately predicts the flow characteristics around these two 5-point stars, where shockwave position, pressure and temperature jumps are accurately captured.

In addition, the pressure distributions on these two 5-point stars' surface are shown in Fig. 14. It is evident from Fig. 14 that the present results are in a good agreement with the body-fitted results, indicating that flow details around two 5-point stars are accurately captured. These numerical results demonstrate the capability and accuracy of the proposed diffuse interface IBM for simulations of compressible viscous flows past solid objects with complex geometries.

4.5. Supersonic flow past the Apollo command module

In this subsection, the proposed diffuse interface IBM is employed to simulate the supersonic flow past the Apollo Command Module. The parameters of this problem are set as: $Ma_\infty = 2$, $Re_\infty = \rho_\infty u_\infty D/\mu = 300$ and $\alpha = 17.8°$. The details of the Apollo Command Module can be found in Ref. [47], and the geometry is shown in Fig. 15(a). As shown in Fig. 15(a), there is a detached bow shock before the Apollo Command Module and a flow recirculation region at the upper side of the module generated by the attack angle. Fig. 15(b) quantitatively compares the surface pressure distribution provided by the present IBM with the body-fitted results, in which good agreements can be observed; it demonstrates that the present method can precisely predict local flow characteristics

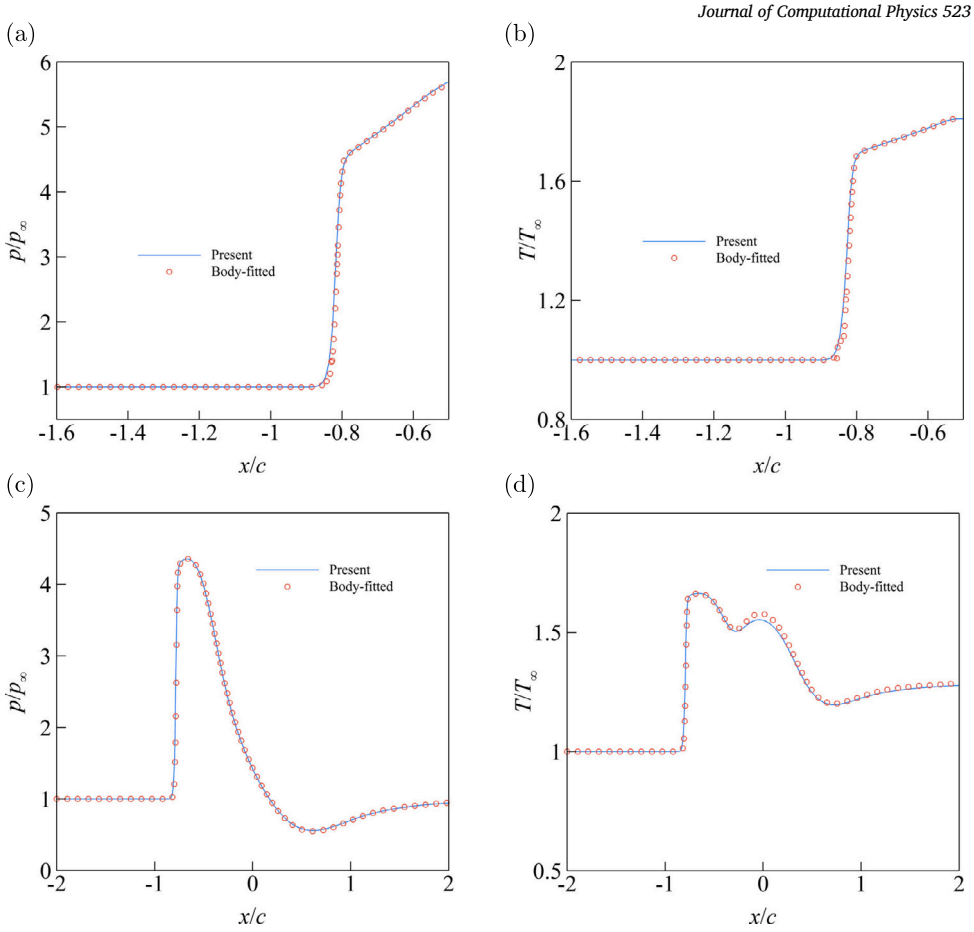

Fig. 10. The pressure and temperature profiles along the stagnation line ($y/c = 0$, first row) and the upward line ($y/c = 0.3$, second row), where the stagnation point is located at $x/c = -0.5$.

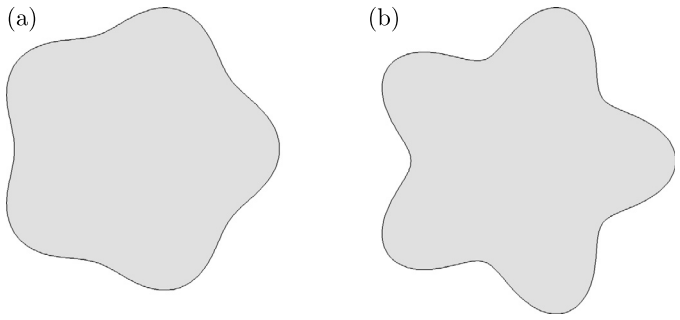

Fig. 11. The geometries of 5-point stars at (a) $\Delta r = 0.05$ and (b) $\Delta r = 0.1$.

around complex geometries. In the Fig. 16, the comparisons of pressure, density, u-velocity and v-velocity contours between present results and body-fitted results are presented. It is evident from Fig. 16 that the results predicted by the proposed diffuse interface IBM are in a good agreement with the body-fitted results, where the re-circulation bubble and shockwave position are accurately captured, qualitatively demonstrating that the global flow characteristics are reproduced by the proposed diffuse interface IBM.

To quantitatively examine the accuracy of the present method, comparisons of pressure and temperature profiles along the forward line ($y/D = 0$) and the upward line ($y/D = 1$) between the present results and body-fitted results are exhibited in Fig. 17. The profiles predicted by the proposed diffuse interface IBM are consistent with those of the body-fitted method, and the local flow configurations, such as shockwave position, pressure and temperature jumps, are accurately predicted.

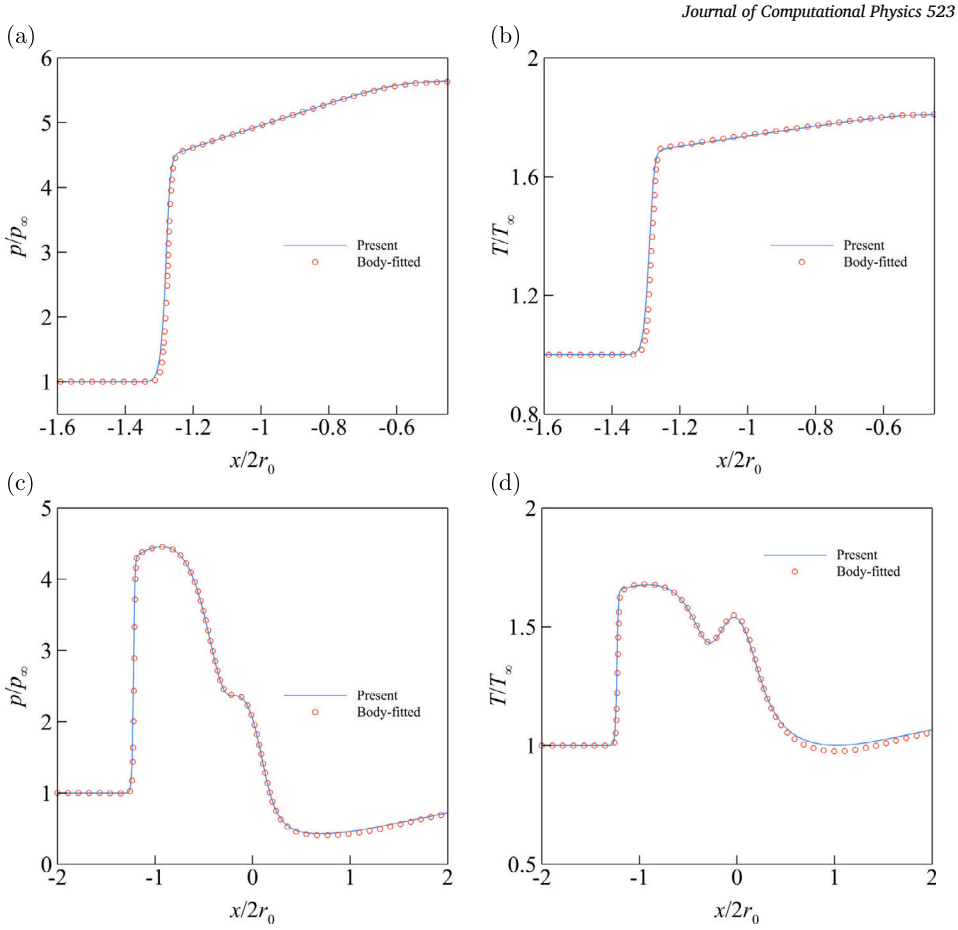

Fig. 12. The pressure and temperature profiles along the stagnation line ($y/2r_0 = 0$, first row) and the upward line ($y/2r_0 = 0.6$, second row) at $\Delta r = 0.05$, where the stagnation point is located at $x/2r_0 = -0.45$.

4.6. Compressible flow past a NACA0012 airfoil

In this subsection, compressible flow past a NACA0012 airfoil is simulated to verify the accuracy and feasibility of the present method. Three classic tests are conducted across subsonic and supersonic flows, with the parameters as follows: (1) $Ma_\infty = u_\infty/c_\infty = 0.8$, $Re_\infty = \rho_\infty u_\infty c/\mu = 500$, and $\alpha = 10°$; (2) $Ma_\infty = 0.5$, $Re_\infty = 5000$, and $\alpha = 0°$; (3) $Ma_\infty = 2$, $Re_\infty = 1000$, and $\alpha = 10°$; where c denotes the chord length. The leading edge of the NACA0012 airfoil is located at the origin and the size of the computational domain is $[-11c, 17c] \times [-11c, 11c]$, with the flow region around the airfoil uniformly discretized at a mesh spacing of $c/500$. To construct a proper correlation between the Eulerian and Lagrangian points, 1000 Lagrangian points are employed to discretize the solid boundary.

Fig. 18 compares the streamlines around the NACA0012 airfoil between the present results and body-fitted solutions. At $Ma_\infty = 0.8$, $Re_\infty = 500$ and $\alpha = 10°$, a large separation region forms on the upper surface of the airfoil, with this vortical structure extending across more than 50% of the chord length on the upper surface, which is consistent with the phenomenon reported by Jawahar and Kamath [48]. The streamlines around the trailing edge of the NACA0012 airfoil are shown in Fig. 18(c) at $Ma_\infty = 0.5$, $Re_\infty = 5000$ and $\alpha = 0°$, where the Reynolds number is near the upper limit of steady laminar flow. It can be seen that flow separation occurs near the trailing edge and a pair of symmetric recirculation bubbles appear in the wake region, which agree well with the observations by Swanson and Langer [49]. These numerical results qualitatively demonstrate the capability and feasibility of the present method for simulating compressible flows with complex geometries.

To quantitatively evaluate the accuracy of the proposed method, the comparison of the pressure distribution on the airfoil surface is shown in Fig. 19. It can be seen that the pressure distributions predicted by the present IBM agree well with reference solutions generated by body-fitted techniques [48] and sharp interface IBM [50], quantitatively indicating that the present method can accurately predict the nonlinear characteristics in compressible flows with complex geometries. To further examine the capability and accuracy of the present method in predicting aerodynamic forces, the drag and lift coefficients are tabulated in Table 2. It is evident from Table 2 that the predicted force coefficients agree well with reference data, further demonstrating that the present method can accurately predict aerodynamic forces for compressible flows.

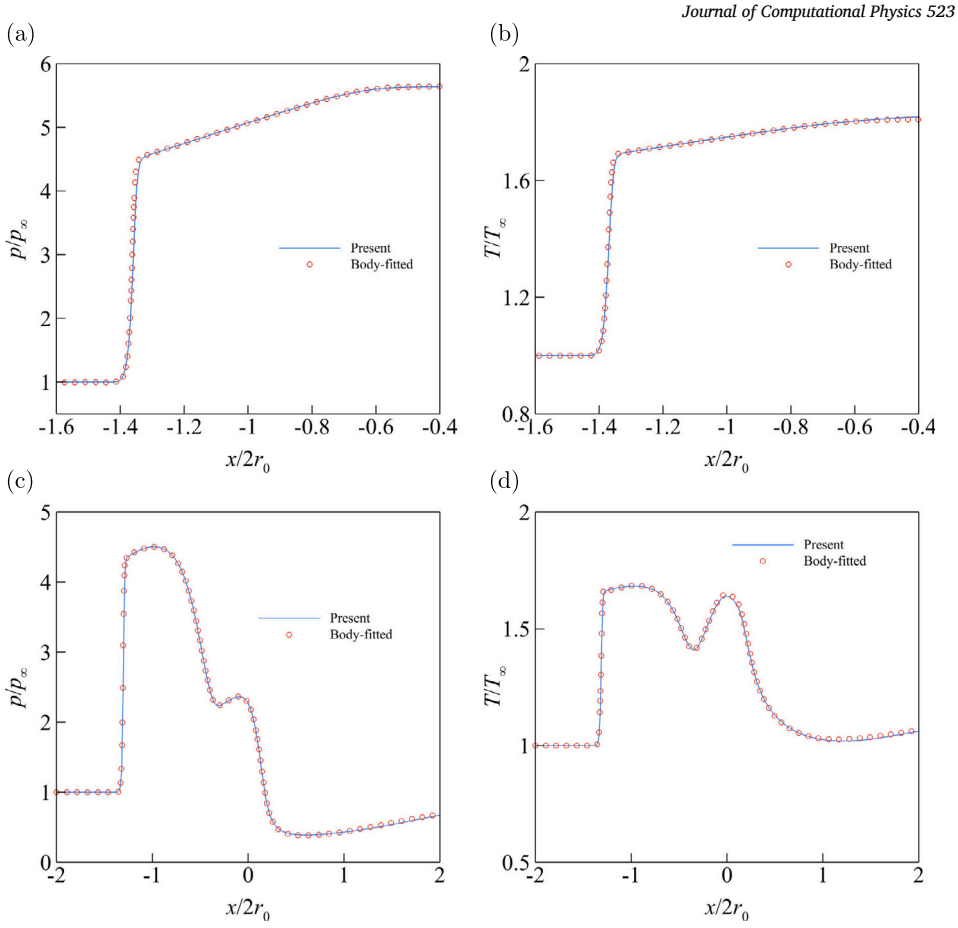

Fig. 13. The pressure and temperature profiles along the stagnation line ($y/2r_0 = 0$, first row) and the upward line ($y/2r_0 = 0.6$, second row) at $\Delta r = 0.1$, where the stagnation point is located at $x/2r_0 = -0.4$.

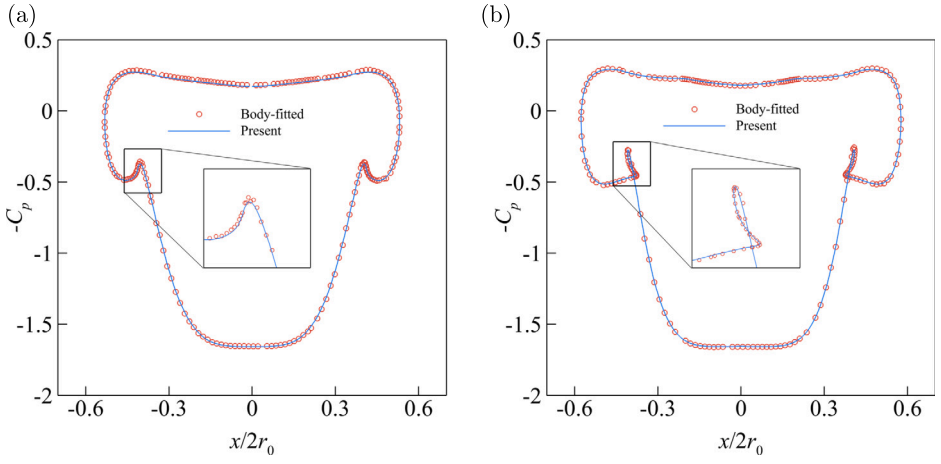

Fig. 14. Pressure distribution on the two 5-point stars' surface at (a) $\Delta r = 0.05$ and (b) $\Delta r = 0.1$.

To globally evaluate the accuracy and capability of the present method for simulating compressible flows, comparisons of pressure, density, u-velocity and v-velocity contours between present results and body-fitted results for the three test cases are presented in Figs. 20, 21 and 22. It can be seen that the flow fields predicted by the proposed one-side diffuse interface IBM are in good agreement with those generated by the body-fitted method, where the recirculation bubble in two subsonic cases and shockwave position in the supersonic case are accurately captured, demonstrating that the proposed IBM can accurately predict global flow characteristics from

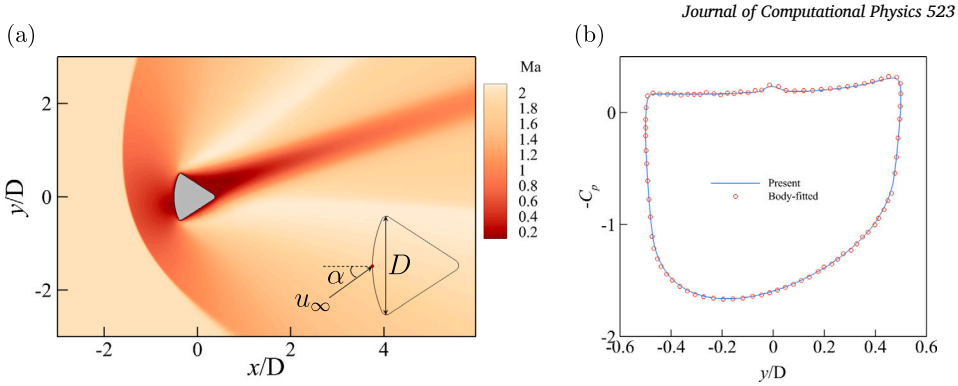

Fig. 15. (a) The Mach contours of supersonic flows past the Apollo Command Module, where α denotes the angle of attack and D represents the characteristic length; the leading point (red point) is located at $(-0.5D, 0)$; (b) the pressure distribution on the surface of the Apollo Command Module. (For interpretation of the colors in the figure(s), the reader is referred to the web version of this article.)

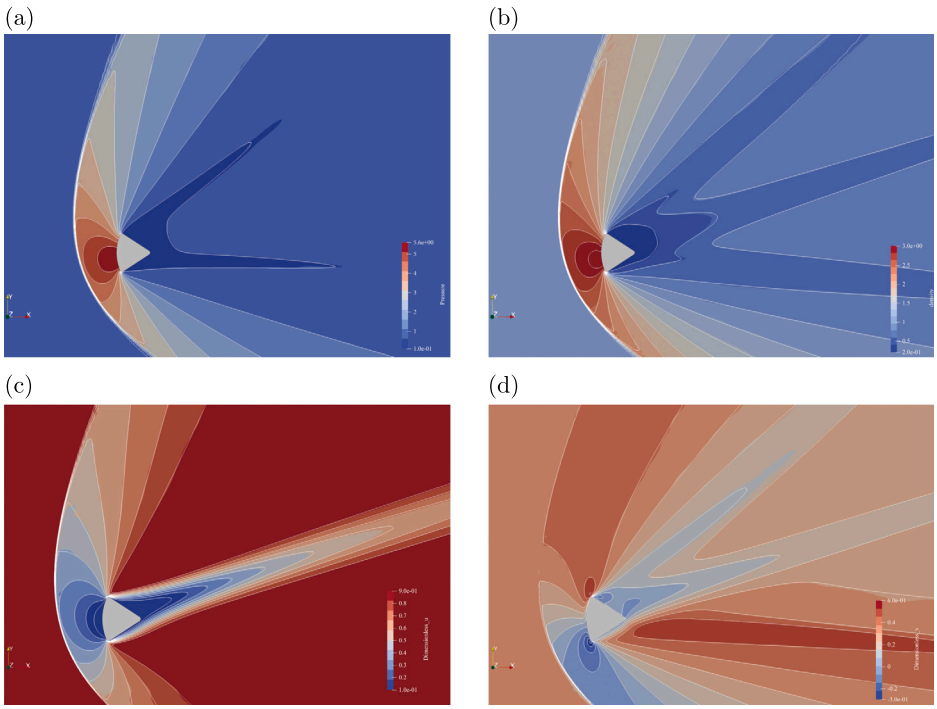

Fig. 16. Comparisons of (a) pressure, (b) density, (c) u-velocity and (d) v-velocity contours between the present results (white solid lines) and the body-fitted results (background contours) at $Ma_\infty = 2.0$ and $Re_\infty = 300$.

Table 2
Comparison of drag C_d and lift C_l coefficients for the compressible flow past a NACA0012 airfoil.

Case	Reference	C_d	C_l
$Ma_\infty = 0.8$,	Jawahar and Kamath [48]	0.27216	0.49394
$Re_\infty = 500$,	Bristeau [51]	0.243-0.2868	0.4145-0.5170
$\alpha = 10°$	Present	0.2796	0.4456
$Ma_\infty = 0.5$,	Jawahar and Kamath [48]	0.05557	0.0
$Re_\infty = 5000$,	Mavriplis and Jameson [52]	0.0561	0.0
$\alpha = 0°$	Present	0.0560	0.0
$Ma_\infty = 2$,	Bristeau [51]	0.2515-0.2535	0.3388-0.3427
$Re_\infty = 1000$,	Forsyth and Jiang [53]	0.2548	0.3407
$\alpha = 10°$	Present	0.2622	0.3358

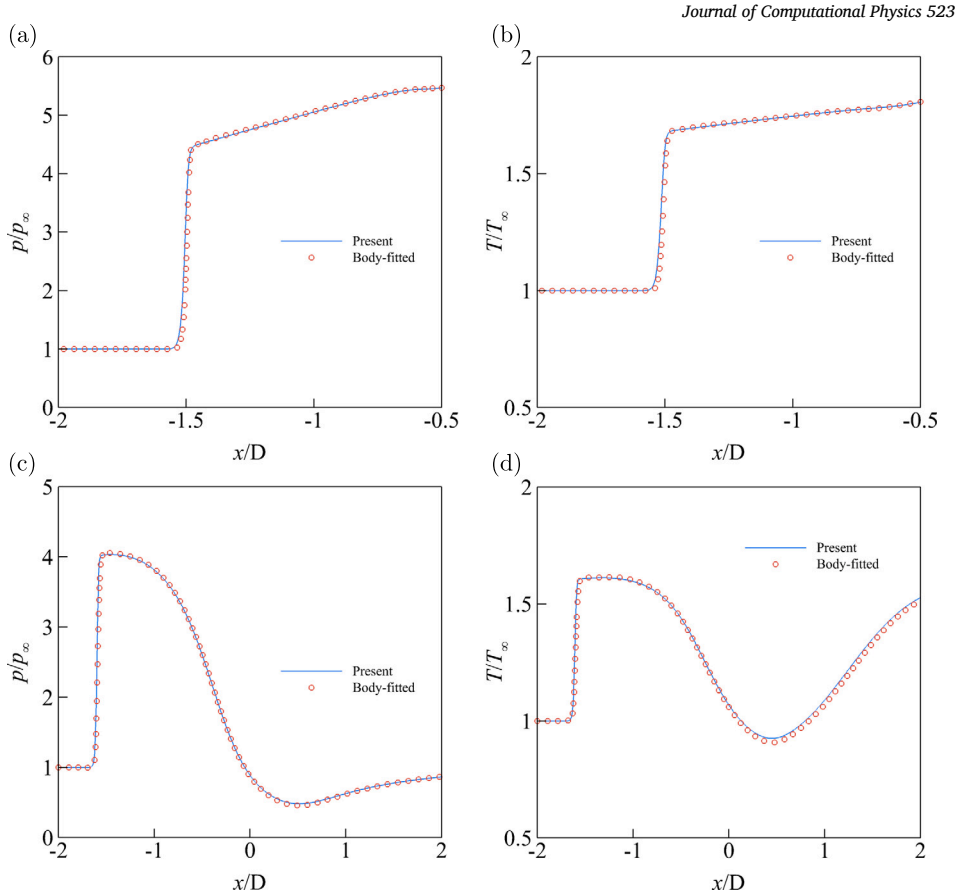

Fig. 17. The pressure and temperature profiles along the forward line ($y/D = 0$, first row) and the upward line ($y/D = 1$, second row) at $Ma_\infty = 2.0$ and $Re_\infty = 300$, where the stagnation point is located at $x/D = -0.5$.

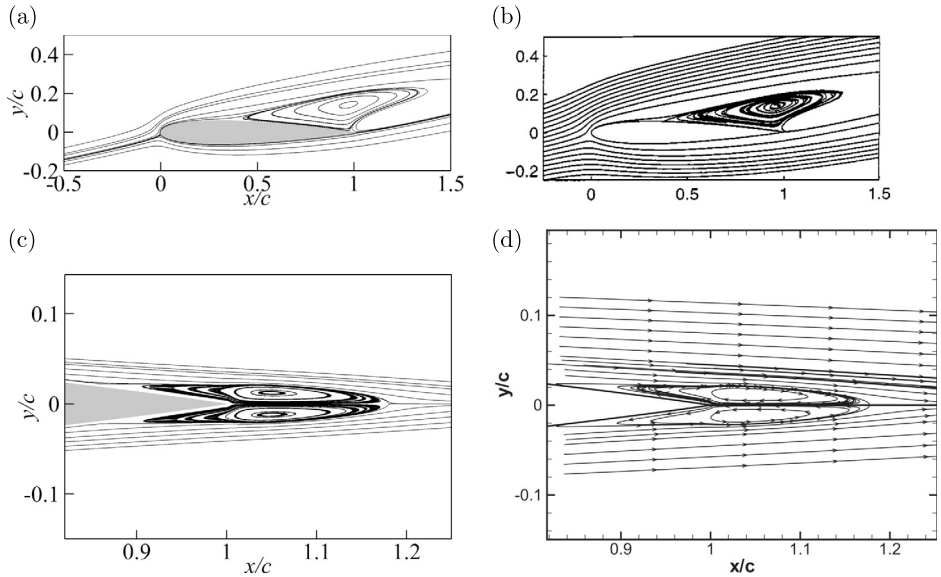

Fig. 18. Comparisons of streamlines between the present results (left column) and reference data (right column). First row: $Ma_\infty = 0.8$, $Re_\infty = 500$ and $\alpha = 10°$; second row: $Ma_\infty = 0.5$, $Re_\infty = 5000$ and $\alpha = 0°$. Figs. 18(b) and 18(d) are generated by body-fitted methods in Jawahar and Kamath [48] and Swanson and Langer [49], respectively.

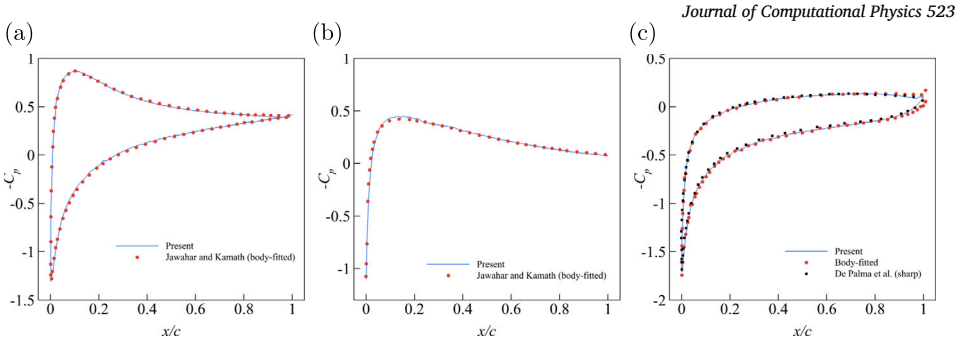

Fig. 19. Pressure distributions on the NACA0012 airfoil at (a) $Ma_\infty = 0.8$, $Re_\infty = 500$ and $\alpha = 10°$, (b) $Ma_\infty = 0.5$, $Re_\infty = 5000$ and $\alpha = 0°$, and (c) $Ma_\infty = 2$, $Re_\infty = 1000$ and $\alpha = 10°$.

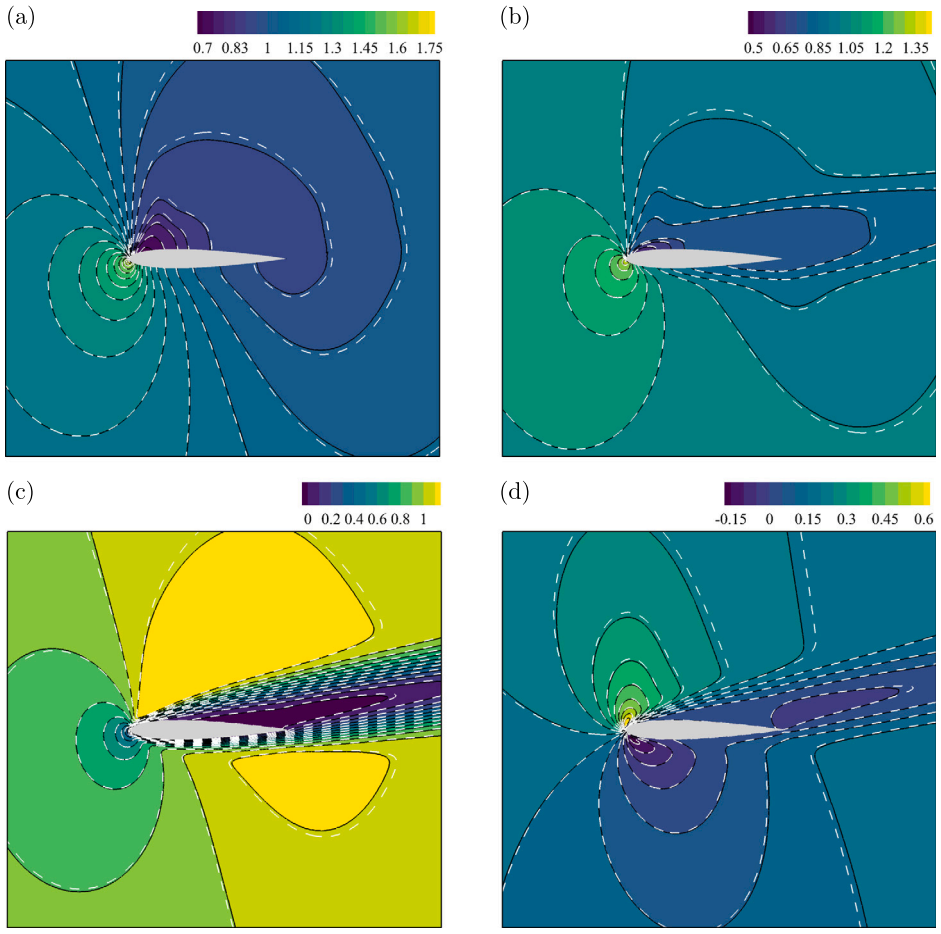

Fig. 20. Comparisons of (a) pressure, (b) density, (c) u-velocity and (d) v-velocity contours between the present results (white dash lines) and the body-fitted results (background contours with black solid lines) at $Ma_\infty = 0.8$, $Re_\infty = 500$ and $\alpha = 10°$.

subsonic to supersonic flows. Note that the flow variables distributions in the region far away from the NACA0012 airfoil exhibit slight deviations from the body-fitted results. These discrepancies may be attributed to the different mesh configurations, farfield boundary conditions, and domain sizes employed in the respective simulations. Moreover, to quantitatively examine the accuracy and capability of the present IBM in predicting the shockwave position, comparisons of pressure and temperature profiles along the forward line ($y/c = 0$) between the present results and body-fitted results are presented in Fig. 23. It is evident from Fig. 23 that the profiles predicted by the present IBM are consistent with those from body-fitted meshes, where the shockwave position, pressure and temperature jumps are accurately captured.

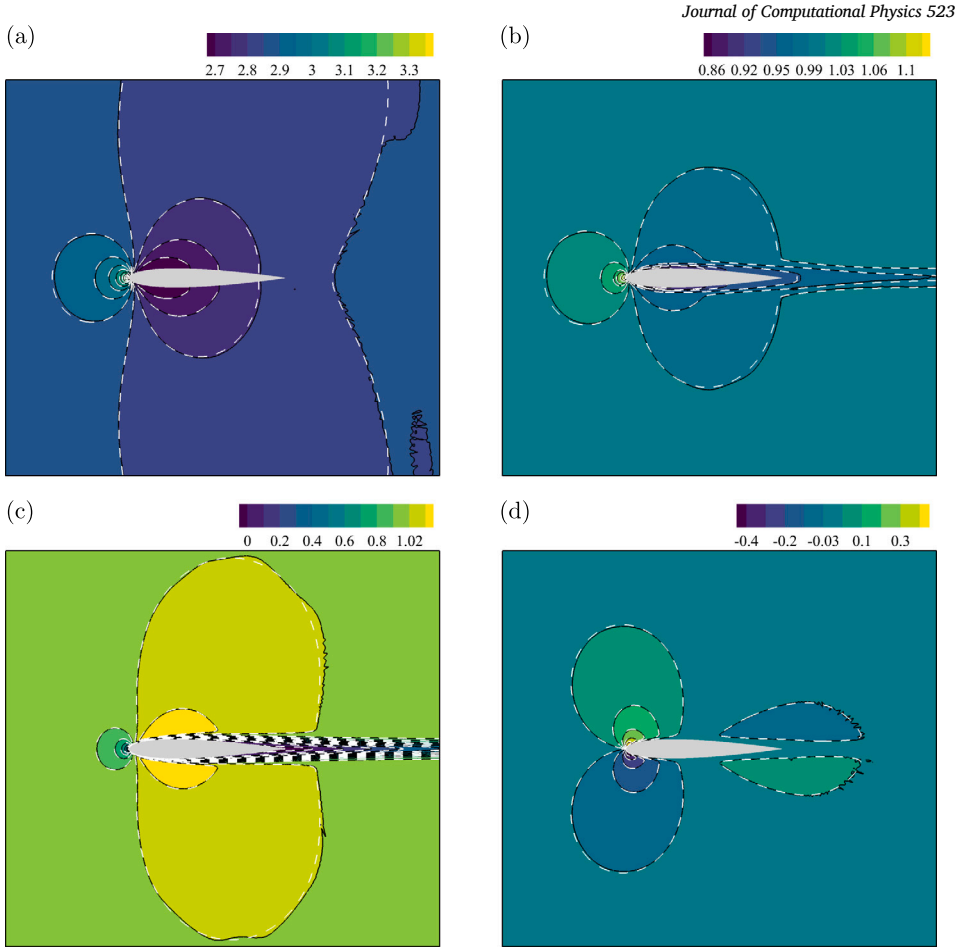

Fig. 21. Comparisons of (a) pressure, (b) density, (c) u-velocity and (d) v-velocity contours between the present results (white dash lines) and the body-fitted results (background contours with black solid lines) at $Ma_\infty = 0.5$, $Re_\infty = 5000$ and $\alpha = 0°$.

4.7. Compressible flow around a moving circular cylinder

In this subsection, to assess the accuracy and capability of the proposed one-side diffuse interface IBM in simulating compressible flows with moving boundaries, the supersonic flow past a circular cylinder (described in Section 4.3) is repeated in a different reference frame with $Ma_\infty = 2.0$ and $Re_\infty = 300$, where a circular cylinder moving through a stationary compressible viscous fluid is simulated. Comparing results from these two reference frames has been widely used to evaluate the capability of the sharp interface IBM in simulating compressible flows with moving boundaries [54,55]. The computational domain size is $[-70D, 10D]\times[-15D, 15D]$, which is discretized by a non-uniform mesh of 6301×271. To save computational costs, the moving region of $[-61D, D]\times[-0.8D, 0.8D]$ is uniformly discretized with a mesh spacing of $h = D/100$. The center of the circular cylinder is moving from $(0, 0)$ to $(-60, 0)$ with a constant velocity $(-u_\infty, 0)$.

Fig. 24 shows the comparisons of pressure, density, u-velocity and v-velocity contours between the moving and stationary reference frames. Note that, for velocity contours of the moving cylinder, the velocity values are calculated in the reference frame fixed on the moving cylinder. It is evident from Fig. 24 that the results obtained in the moving reference frame are almost identical to those from the stationary reference frame, qualitatively indicating the capability and feasibility of the present method for simulating moving objects in a strongly compressible environment.

Furthermore, to quantitatively evaluate the accuracy of the present method for addressing compressible moving-boundary problems, the pressure profile along the stagnation line and the pressure distribution on the cylinder surface are presented in Fig. 25. It can be seen that the results from the moving reference frame agree well with both the reference data [39,46] and those from the stationary reference frame, demonstrating that the proposed one-side diffuse interface IBM can accurately predict the flow characteristics, such as the shockwave position and pressure jump, for compressible flows with moving boundaries. Moreover, the drag coefficient C_d and the shock stand-off distance Δs are presented in Table 3. The numerical results predicted by the present method agree well with those of Ménez et al. [39], and the numerical solutions from the moving reference frame are identical to those from the stationary reference frame. These numerical observations further demonstrate the accuracy and capability of the proposed IBM for compressible moving-boundary problems.

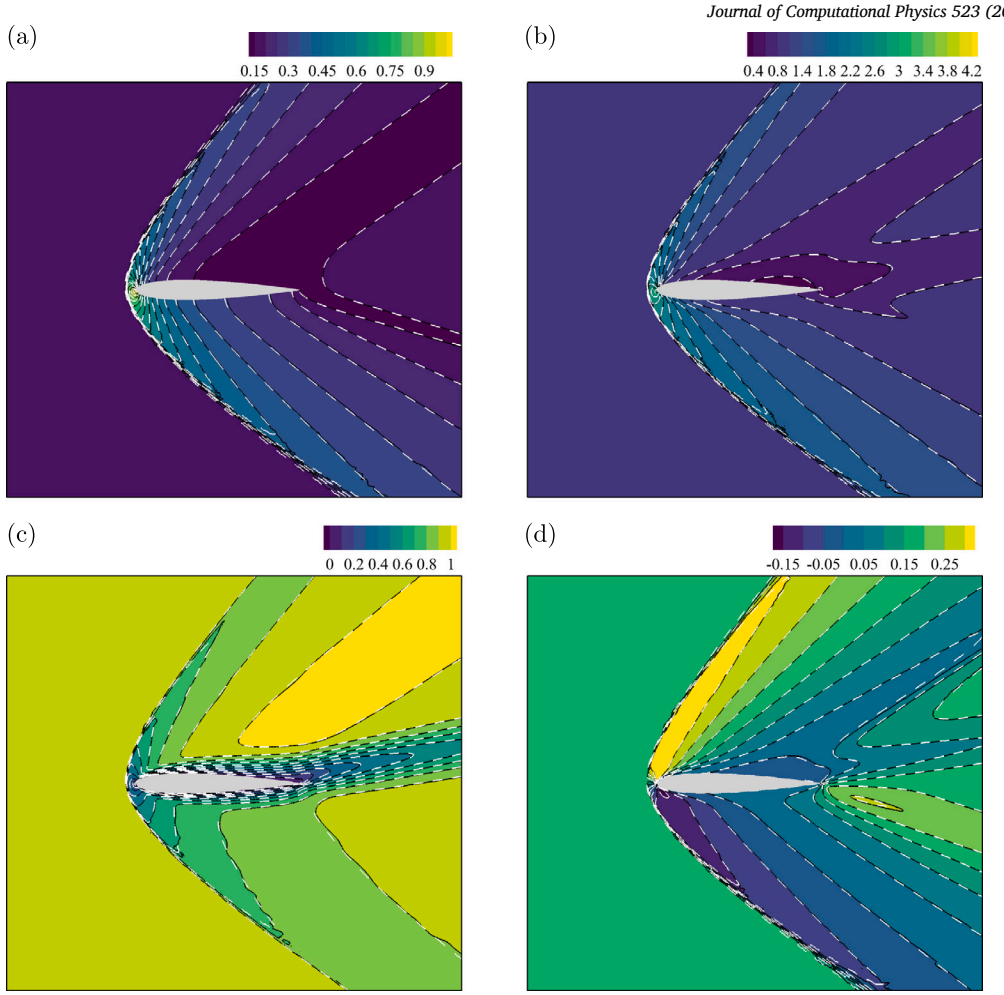

Fig. 22. Comparisons of (a) pressure, (b) density, (c) u-velocity and (d) v-velocity contours between the present results (white dash lines) and the body-fitted results (background contours with black solid lines) at $Ma_\infty = 2.0$, $Re_\infty = 1000$ and $\alpha = 10°$.

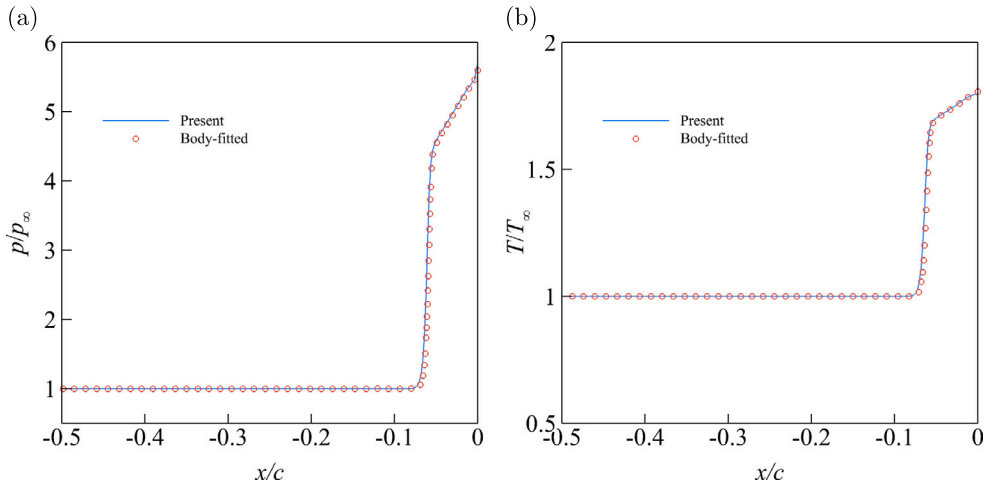

Fig. 23. The pressure and temperature profiles along the forward line ($y/c = 0$) at $Ma_\infty = 2.0$, $Re_\infty = 1000$ and $\alpha = 10°$, where the stagnation point is located at $x/c = 0$.

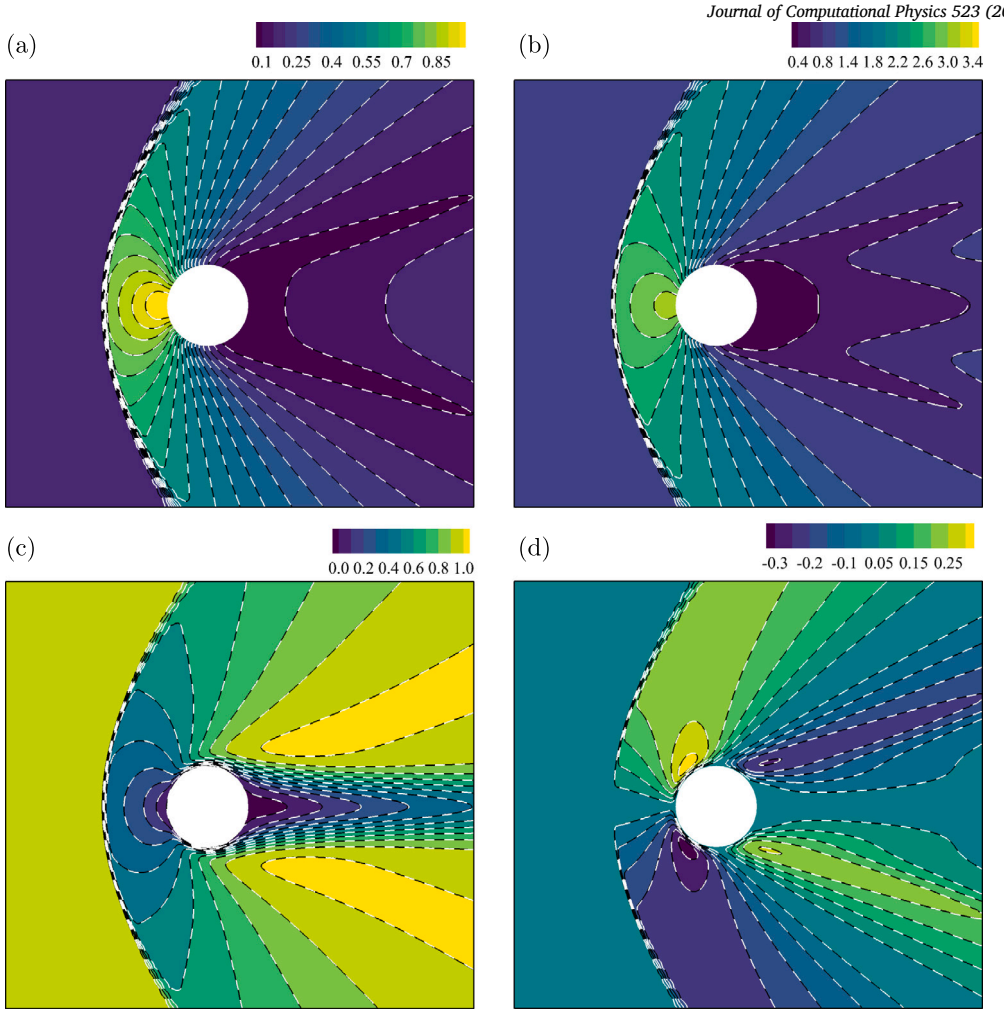

Fig. 24. Comparisons of (a) pressure, (b) density, (c) u-velocity and (d) v-velocity contours between the moving (background contours with black solid lines) and stationary (white dash lines) reference frames at $Ma_\infty = 2.0$ and $Re_\infty = 300$.

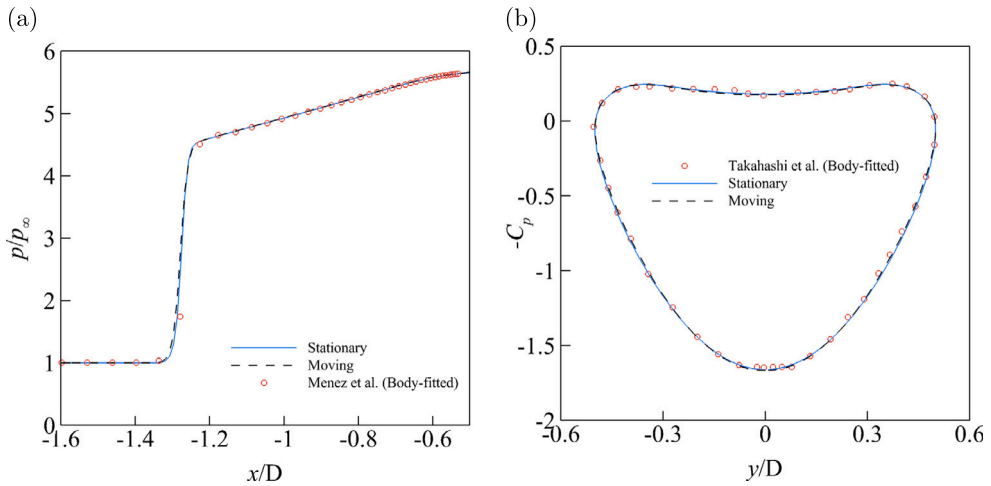

Fig. 25. (a) Pressure profile along the stagnation line ($y/D = 0$), where the center of the moving cylinder is relocated at $(0,0)$ for easy comparison. (b) Pressure distribution on the surface of the circular cylinder.

Table 3
Comparison of the drag coefficient C_d and the shock stand-off distance Δs for the moving and stationary reference frames at $Ma_\infty = 2.0$ and $Re_\infty = 300$.

Reference	C_d	Δs
Ménez et al. [39], diffuse	1.59	0.73
Ménez et al. [39], body-fitted	1.62	0.73
Ménez et al. [39], sharp	1.60	0.72
Present (stationary, $h = D/100$)	1.62	0.74
Present (moving, $h = D/100$)	1.62	0.74

5. Conclusions

In the present work, a novel one-side diffuse-interface immersed boundary method is proposed for simulating compressible viscous flows around complex geometries, where two linear systems are constructed to accurately enforce the Dirichlet and Neumann boundary conditions on the immersed object, respectively. To eliminate the non-physical pressure jump introduced by the diffusion effects from the regularization delta function, a novel spreading scheme for distributing the Lagrangian corrections on the surrounding Eulerian points inside the solid domain is incorporated with the proposed diffuse IBM. Furthermore, the proposed diffuse interface IBM is integrated with the gas kinetic flux solver (GKFS) to resolve the compressible flow characteristics around the immersed object, in which the fractional-step method is employed to decouple the Navier-Stokes equations into the prediction and correction steps. In the prediction step, the intermediate flow variables are predicted by the GKFS without considering the IBM restoring forcing terms. Subsequently, in the correction step, the proposed diffuse interface IBM is adopted to evaluate the flow variable corrections for achieving the desired boundary conditions.

The one-side diffuse-interface IBM is validated with several numerical benchmarks. The supersonic flow past an adiabatic circular cylinder is adopted to examine the accuracy of the proposed numerical approach, and the results indicate that the overall spatial accuracy is second-order. Subsequently, two numerical cases of supersonic flow over a circular cylinder with isothermal and adiabatic boundary conditions are adopted to evaluate the accuracy and capability of the proposed numerical approach for compressible flow. The boundary errors are negligible and close to machine round-off, demonstrating that the physical boundary conditions are accurately implemented by the present diffuse interface IBM. The numerical results show that the non-physical pressure jump in the previous study is eliminated by the proposed IBM, and the resolved pressure and temperature profiles are in a good agreement with the results of the sharp interface method and the body-fitted approach. Specifically, the previous studies show that the pressure distributions on the leeward side generated by the existing diffuse interface IBMs have some discrepancies with the body-fitted results. In contrast, the pressure distributions on the cylinder surface predicted by the present diffuse interface IBM agree well with the body-fitted results at different Mach numbers, indicating that the flow characteristics around the immersed object are accurately predicted. To further examine the capability and flexibility of the proposed method for complex geometries, the supersonic flow past an ellipse cylinder and two different 5-point stars are conducted. The numerical results show that the shockwave positions, the temperature profiles, and the pressure distributions on the immersed surface are in a good agreement with the body-fitted results. Lastly, the proposed diffuse IBM is extended to simulate the supersonic flow over the Apollo Command Module, where the pressure, density and velocity contours are consistent with the body-fitted results. These numerical observations indicate the proposed diffuse interface IBM can accurately predict the local and global flow characteristics of compressible flows around complex geometries.

CRediT authorship contribution statement

Buchen Wu: Writing – review & editing, Writing – original draft, Visualization, Validation, Software, Methodology, Investigation, Formal analysis, Data curation, Conceptualization. **Yaguang Liu:** Validation, Software, Data curation, Visualization, Writing – original draft. **Lin Fu:** Writing – review & editing, Writing – original draft, Supervision, Software, Resources, Project administration, Methodology, Investigation, Funding acquisition, Formal analysis, Conceptualization.

Declaration of competing interest

The authors declare that they have no known competing financial interests or personal relationships that could have appeared to influence the work reported in this paper.

Acknowledgements

Lin Fu acknowledges the fund from National Natural Science Foundation of China (No. 12422210), the fund from the Research Grants Council (RGC) of the Government of Hong Kong Special Administrative Region (HKSAR) with RGC/ECS Project (No. 26200222), RGC/GRF Project (No. 16201023) and RGC/STG Project (No. STG2/E-605/23-N), the fund from Guangdong Basic and Applied Basic Research Foundation (No. 2024A1515011798), the fund from Guangdong Province Science and Technology Plan Project (No. 2023A0505030005), and the fund from the Project of Hetao Shenzhen–Hong Kong Science and Technology Innovation Cooperation Zone (No. HZQB-KCZYB-2020083). Buchen Wu would like to acknowledge Dr. Yu Sun for his kind assistance in preparing this work.

Data availability

Data will be made available on request.

References

[1] C.S. Peskin, Numerical analysis of blood flow in the heart, J. Comput. Phys. 25 (1977) 220–252.
[2] Z.-G. Feng, E.E. Michaelides, The immersed boundary-lattice Boltzmann method for solving fluid–particles interaction problems, J. Comput. Phys. 195 (2004) 602–628.
[3] Z.-G. Feng, E.E. Michaelides, Proteus: a direct forcing method in the simulations of particulate flows, J. Comput. Phys. 202 (2005) 20–51.
[4] D. Goldstein, R. Handler, L. Sirovich, Modeling a no-slip flow boundary with an external force field, J. Comput. Phys. 105 (1993) 354–366.
[5] L. Zhu, G. He, S. Wang, L. Miller, X. Zhang, Q. You, S. Fang, An immersed boundary method based on the lattice Boltzmann approach in three dimensions, with application, Comput. Math. Appl. 61 (2011) 3506–3518.
[6] J. Mohd-Yusof, Combined immersed-boundary/b-spline methods for simulations of flow in complex geometries, Center for Turbulence Research Annual Research Briefs 161 (1997) 317–327.
[7] E. Fadlun, R. Verzicco, P. Orlandi, J. Mohd-Yusof, Combined immersed-boundary finite-difference methods for three-dimensional complex flow simulations, J. Comput. Phys. 161 (2000) 35–60.
[8] M. Uhlmann, An immersed boundary method with direct forcing for the simulation of particulate flows, J. Comput. Phys. 209 (2005) 448–476.
[9] S.-W. Su, M.-C. Lai, C.-A. Lin, An immersed boundary technique for simulating complex flows with rigid boundary, Comput. Fluids 36 (2007) 313–324.
[10] M. Jiang, Z. Liu, A boundary thickening-based direct forcing immersed boundary method for fully resolved simulation of particle-laden flows, J. Comput. Phys. 390 (2019) 203–231.
[11] B. Wu, H. Lee, C. Shu, M. Wan, Explicit boundary thickening direct forcing immersed boundary method, Int. J. Mech. Sci. 270 (2024) 109063.
[12] K. Luo, Z. Wang, J. Fan, K. Cen, Full-scale solutions to particle-laden flows: multidirect forcing and immersed boundary method, Phys. Rev. E 76 (2007) 066709.
[13] Z. Wang, J. Fan, K. Luo, Combined multi-direct forcing and immersed boundary method for simulating flows with moving particles, Int. J. Multiph. Flow 34 (2008) 283–302.
[14] S.K. Kang, Y.A. Hassan, A comparative study of direct-forcing immersed boundary-lattice Boltzmann methods for stationary complex boundaries, Int. J. Numer. Methods Fluids 66 (2011) 1132–1158.
[15] T. Kempe, J. Fröhlich, An improved immersed boundary method with direct forcing for the simulation of particle laden flows, J. Comput. Phys. 231 (2012) 3663–3684.
[16] J. Wu, C. Shu, Implicit velocity correction-based immersed boundary-lattice Boltzmann method and its applications, J. Comput. Phys. 228 (2009) 1963–1979.
[17] J. Wu, C. Shu, An improved immersed boundary-lattice Boltzmann method for simulating three-dimensional incompressible flows, J. Comput. Phys. 229 (2010) 5022–5042.
[18] B. Wu, J. Lu, H. Lee, C. Shu, M. Wan, An explicit immersed boundary-reconstructed thermal lattice Boltzmann flux solver for thermal–fluid-structure interaction problems, Int. J. Mech. Sci. 235 (2022) 107704.
[19] B. Wu, J. Lu, H. Lee, C. Shu, M. Wan, An efficient explicit immersed boundary-reconstructed lattice Boltzmann flux solver for isothermal fluid-structure interaction problems with large deformations and complex geometries, Appl. Math. Model. 114 (2023) 627–645.
[20] R. Mittal, R. Bhardwaj, Immersed boundary methods for thermofluids problems, Annu. Rev. Heat Transf. 24 (2021).
[21] B. Wu, C. Shu, M. Wan, Y. Wang, S. Chen, Hydrodynamic performance of an unconstrained flapping swimmer with flexible fin: a numerical study, Phys. Fluids 34 (2022) 011901.
[22] B. Wu, C. Shu, H. Lee, M. Wan, The effects of caudal fin's bending stiffness on a self-propelled carangiform swimmer, Phys. Fluids 34 (2022) 041901.
[23] B. Wu, C. Shu, H.C. Lee, M. Wan, Numerical study on the hydrodynamic performance of an unconstrained carangiform swimmer, Phys. Fluids 34 (2022) 121902.
[24] L. Kang, S. Xiong, B. Wu, C. Li, M. Ge, D. Yuan, F. Han, W. Cui, Force decomposition on flapping flexible plate via impulse theory and dynamic mode decomposition, Phys. Fluids 35 (2023).
[25] R.J. LeVeque, Z. Li, Immersed interface methods for Stokes flow with elastic boundaries or surface tension, SIAM J. Sci. Comput. 18 (1997) 709–735.
[26] Z. Li, M.-C. Lai, The immersed interface method for the Navier–Stokes equations with singular forces, J. Comput. Phys. 171 (2001) 822–842.
[27] L. Lee, R.J. LeVeque, An immersed interface method for incompressible Navier–Stokes equations, SIAM J. Sci. Comput. 25 (2003) 832–856.
[28] D.K. Clarke, M. Salas, H. Hassan, Euler calculations for multielement airfoils using Cartesian grids, AIAA J. 24 (1986) 353–358.
[29] T. Ye, R. Mittal, H. Udaykumar, W. Shyy, An accurate Cartesian grid method for viscous incompressible flows with complex immersed boundaries, J. Comput. Phys. 156 (1999) 209–240.
[30] M. Kirkpatrick, S. Armfield, J. Kent, A representation of curved boundaries for the solution of the Navier–Stokes equations on a staggered three-dimensional Cartesian grid, J. Comput. Phys. 184 (2003) 1–36.
[31] Y.-H. Tseng, J.H. Ferziger, A ghost-cell immersed boundary method for flow in complex geometry, J. Comput. Phys. 192 (2003) 593–623.
[32] R. Ghias, R. Mittal, H. Dong, A sharp interface immersed boundary method for compressible viscous flows, J. Comput. Phys. 225 (2007) 528–553.
[33] R. Mittal, H. Dong, M. Bozkurttas, F. Najjar, A. Vargas, A. Von Loebbecke, A versatile sharp interface immersed boundary method for incompressible flows with complex boundaries, J. Comput. Phys. 227 (2008) 4825–4852.
[34] Y. Qiu, C. Shu, J. Wu, Y. Sun, L. Yang, T. Guo, A boundary condition-enforced immersed boundary method for compressible viscous flows, Comput. Fluids 136 (2016) 104–113.
[35] L. Wang, G.M. Currao, F. Han, A.J. Neely, J. Young, F.-B. Tian, An immersed boundary method for fluid–structure interaction with compressible multiphase flows, J. Comput. Phys. 346 (2017) 131–151.
[36] Y. Sun, L. Yang, C. Shu, Y. Chen, A diffuse-interface immersed boundary method for simulation of compressible viscous flows with stationary and moving boundaries, Int. J. Numer. Methods Fluids 92 (2020) 149–168.
[37] H. Riahi, M. Meldi, J. Favier, E. Serre, E. Goncalves, A pressure-corrected immersed boundary method for the numerical simulation of compressible flows, J. Comput. Phys. 374 (2018) 361–383.
[38] H. Yu, C. Pantano, An immersed boundary method with implicit body force for compressible viscous flow, J. Comput. Phys. 459 (2022) 111125.
[39] L. Ménez, P. Parnaudeau, M. Beringhier, E.G. Da Silva, Assessment of volume penalization and immersed boundary methods for compressible flows with various thermal boundary conditions, J. Comput. Phys. 493 (2023) 112465.
[40] Y. Sun, C. Shu, C.J. Teo, Y. Wang, L. Yang, Explicit formulations of gas-kinetic flux solver for simulation of incompressible and compressible viscous flows, J. Comput. Phys. 300 (2015) 492–519.
[41] C. Ji, A. Munjiza, J. Williams, A novel iterative direct-forcing immersed boundary method and its finite volume applications, J. Comput. Phys. 231 (2012) 1797–1821.
[42] C. Shu, N. Liu, Y.-T. Chew, A novel immersed boundary velocity correction–lattice Boltzmann method and its application to simulate flow past a circular cylinder, J. Comput. Phys. 226 (2007) 1607–1622.
[43] V. Kumar, A. Sharma, R. Singh, Central upwind scheme based immersed boundary method for compressible flows around complex geometries, Comput. Fluids 196 (2020) 104349.

[44] J.M. Turner, J.H. Seo, R. Mittal, A high-order sharp-interface immersed boundary solver for high-speed flows, J. Comput. Phys. 500 (2024) 112748.
[45] L. Yang, C. Shu, J. Wu, A hybrid lattice Boltzmann flux solver for simulation of viscous compressible flows, Adv. Appl. Math. Mech. 8 (2016) 887–910.
[46] S. Takahashi, T. Nonomura, K. Fukuda, et al., A numerical scheme based on an immersed boundary method for compressible turbulent flows with shocks: application to two-dimensional flows around cylinders, J. Appl. Math. 2014 (2014).
[47] J. Moss, C. Glass, F. Greene, Dsmc simulations of Apollo capsule aerodynamics for hypersonic rarefied conditions, in: 9th AIAA/ASME Joint Thermophysics and Heat Transfer Conference, 2006, p. 3577.
[48] P. Jawahar, H. Kamath, A high-resolution procedure for Euler and Navier–Stokes computations on unstructured grids, J. Comput. Phys. 164 (2000) 165–203.
[49] R. Swanson, S. Langer, Steady-state laminar flow solutions for naca 0012 airfoil, Comput. Fluids 126 (2016) 102–128.
[50] P. De Palma, M. De Tullio, G. Pascazio, M. Napolitano, An immersed-boundary method for compressible viscous flows, Comput. Fluids 35 (2006) 693–702.
[51] M.O. Bristeau, Numerical Simulation of Compressible Navier-Stokes Flows: a GAMM Workshop, vol. 18, Springer Science & Business Media, 2013.
[52] D.J. Mavriplis, A. Jameson, Multigrid solution of the Navier-Stokes equations on triangular meshes, AIAA J. 28 (1990) 1415–1425.
[53] P.A. Forsyth, H. Jiang, Nonlinear iteration methods for high speed laminar compressible Navier-Stokes equations, Comput. Fluids 26 (1997) 249–268.
[54] R. Yuan, C. Zhong, An immersed-boundary method for compressible viscous flows and its application in the gas-kinetic bgk scheme, Appl. Math. Model. 55 (2018) 417–446.
[55] F. De Vanna, F. Picano, E. Benini, A sharp-interface immersed boundary method for moving objects in compressible viscous flows, Comput. Fluids 201 (2020) 104415.